JOURNAL OF GEOPHYSICAL RESEARCH, VOL. , NO. , PAGES 1–21,

Coupled response of the inner magnetosphere and ionosphere on 17 April 2002

J. Goldstein, J. L. Burch

Space Science and Engineering Division, Southwest Research Institute, San Antonio, TX 78228 USA

B. R. Sandel

Lunar and Planetary Laboratory, University of Arizona, Tucson, AZ 85721 USA

S. B. Mende

University of California Berkeley, Space Sciences Laboratory, Berkeley, CA 94720 USA

P. C:son Brandt

Johns Hopkins University Applied Physics Laboratory, Laurel, MD 20723 USA

M. R. Hairston

Center for Space Sciences, University of Texas at Dallas, Richardson, TX 75083 USA

Abstract.

We present an observational study of the global dynamics of the plasmasphere, aurora, ring current, and subauroral ionosphere on 17 April 2002, during a substorm. Global observations by IMAGE and in situ observations by DMSP F13 provide a comprehensive view of the coupled response of the inner magnetosphere and ionosphere. At 1900 UT a substorm onset initiated a sunward convective impulse which caused a ring current injection. The motion of this impulse past the plasmasphere caused ripples to propagate along the plasmapause, eastward and westward from pre-midnight MLT. The motion of the ripples agrees exceptionally well with the motion of the aurora and the ring current, implying strong coupling. The westward-moving ripple (on the duskside) participated in a two-phase plasmapause undulation effect. In the first phase (1915 UT to 1936 UT), a mild 0.4–0.5 R_E bulge formed near 2000 MLT, probably caused by an E-field induced by local reduction of the magnetic field by the ring current pressure increase. In the second phase (1936 UT to 2037 UT) this mild bulge was removed by a sub-auroral polarization stream (SAPS) westward flow that stripped away the outer 1 R_E of the duskside plasmasphere. The SAPS effect was observed in the ionosphere by DMSP between about 1930 UT and 2000 UT, and evident in vector E-fields inferred from plasmapause motion. All the observations of this event suggest strong coupling among the plasma populations of the magnetosphere-ionosphere system. This event represents the first identification of the directly-observed global plasmaspheric effects of a substorm-driven impulse, the SAPS flow channel, and of the ring-current magnetic field reduction.

1. Introduction

The inner magnetosphere and ionosphere respond to the external driving of the solar wind (SW) and interplanetary magnetic field (IMF). There is ample evidence that dayside magnetopause reconnection (DMR) during southward IMF imposes a dawn-dusk electric field that drives sunward convection in the inner magnetosphere and the subauroral ionosphere [*Dungey*, 1961]. Global plasmapause observations by IMAGE EUV have shown a strong correlation between southward IMF intervals, and sunward plasmapause motions [*Goldstein et al.*, 2003a; *Spasojević et al.*, 2003; *Goldstein et al.*, 2003b, 2004b]. It has so far been consistently observed that there is a time delay of 20 to 30 minutes between the IMF polarity transition at the magnetopause, and the corresponding plasmapause motion. *Goldstein et al.* [2003a] hypothesized that this 20–30-minute delay (hereinafter called $\Delta\tau$) consisted mostly of the time required for the global convection field (in both magnetosphere and ionosphere) to reconfigure itself, consistent with the results of *Coroniti and Kennel* [1973]. Whatever the cause, we treat this time delay $\Delta\tau$ as an observational fact.

The dynamics of the inner magnetosphere and ionosphere are also very strongly dependent upon internal processes that are not directly driven by the solar wind and IMF. The auroral substorm is a process that produces dramatic precipitation signatures in the ionosphere [*Akasofu*, 1964]. The

Paper number .
0148-0227/04/$9.00

substorm onset is a sudden brightening of a portion of the most equatorward auroral precipitation in the pre-midnight magnetic local time (MLT) ionosphere. The brightening expands rapidly westward and/or eastward and poleward to form a large auroral oval with internal arc-like structures. The ionospheric conductivity is enhanced by the auroral precipitation that occurs during the substorm [*Harang*, 1951]. The auroral substorm signatures are thought to indicate the state of the larger magnetosphere that is connected to the ionosphere via geomagnetic field lines. At the onset of an auroral substorm, the global nightside magnetic field is believed to reconfigure from a tail-like geometry to a more dipolar geometry (e.g., *Baker et al.* [1996]). The rapid sunward motion of geomagnetic field lines during substorm dipolarization induces a global electric field [*Aggson et al.*, 1983] which transports magnetotail plasma earthward and energizes it, a process called 'injection.' Injections produce sharp increases in ring current particle fluxes [*Arnoldy and Chan*, 1969; *Walker et al.*, 1976; *Baker et al.*, 1982], and observations indicate that the injection front approaches from the pre-midnight MLT sector [*McIlwain*, 1974; *Vagina et al.*, 1996]. The triggering of substorm onset probably depends on both external driving by the SW and IMF [*Lyons*, 1995], and on internal processes involving magnetosphere-ionosphere coupling (e.g., *Kan and Sun* [1996]; *Lui* [1996]). There is good evidence that substorm dipolarization provides a strong sunward push to the plasmaspheric plasma (e.g., *Carpenter and Smith* [2001] and references therein).

Another important internal process of the magnetosphere-ionosphere system is the subauroral polarization stream (SAPS), also known as subauroral ion drift (SAID) or polarization jet. SAPS is a disturbance-time effect in which feedback between the ring current and ionosphere produces an intense, radially confined, westward flow region in the dusk-to-midnight MLT sector [*Foster and Burke*, 2002; *Foster et al.*, 2002; *Foster and Vo*, 2002; *Anderson et al.*, 2001; *Burke et al.*, 1998, 2000]. Ionospheric SAPS occur when the equatorward boundaries of the ion and electron plasma sheets separate in the dusk-to-midnight MLT sector, leading to a poleward-flowing Pedersen current in the subauroral ionosphere. Because of the low conductivity in the subauroral ionosphere, the poleward Pedersen current generates an intense poleward E-field that is then mapped via geomagnetic field lines to a strong radial E-field in the equatorial plane between the ion and electron plasma sheet edges. SAPS forms a radially narrow (1 to 2 $R_{\rm E}$ wide) flow channel just outside or overlapping the dusk-to-midnight plasmasphere. The presence of this SAPS flow channel has been demonstrated to play an important role in duskside plasmaspheric dynamics by intensifying sunward convection there, producing decreased plasmapause radius and at times creating narrow duskside plumes [*Foster et al.*, 2002; *Goldstein et al.*, 2003b, 2004b, a].

The Imager for Magnetopause-to-Aurora Global Exploration (IMAGE) mission is the first satellite mission dedicated to imaging the Earth's magnetosphere [*Burch*, 2000]. IMAGE uses a combination of ultraviolet and neutral atom imaging to obtain a global picture of three distinct plasma populations: (1) The plasmasphere is captured by the extreme ultraviolet (EUV) imager [*Sandel et al.*, 2000], (2) auroral precipitating electrons are observed by the far ultraviolet (FUV) imager [*Mende et al.*, 2000], and (3) the ring current is viewed by the high-energy neutral atom (HENA) imager [*Mitchell et al.*, 2000].

In situ measurements complement the overall global picture provided by IMAGE data. The Defense Meteorological Satellite Program (DMSP) [*Rich and Hairston*, 1994] obtains particle flux, ion drift-meter, and magnetometer data in the subauroral ionosphere at 850 km altitude. The Advanced Composition Explorer (ACE) [*Stone et al.*, 1998] provides continuous monitoring of the solar wind (SW) and interplanetary magnetic field (IMF).

In this paper we study the global dynamics of the plasmasphere, aurora, ring current and subauroral ionosphere on 17 April 2002, during 1800–2100 UT. On this day, a mild geomagnetic storm occurred (see next section and Figure 1). In the time interval 1800–2100 UT, IMAGE observations show a very striking undulatory motion of the plasmapause, in which a large ripple propagated westward from pre-midnight across the duskside plasmapause, and a smaller ripple propagated eastward along the dawnside plasmapause [*Goldstein et al.*, 2004a]. This plasmapause motion was part of a larger global sunward motion of inner magnetospheric plasma, apparently associated with a substorm onset and simultaneous ring current injection that occurred at about 1900 UT. The substorm and ring current injection apparently triggered the formation of a SAPS flow channel that stripped away the outer edge of the duskside plasmapause, producing the westward-propagating ripple. We present a more comprehensive follow-up to the brief report of *Goldstein et al.* [2004a] of the coupled response of the inner magnetosphere and ionosphere during this 17 April 2002 event. Our study of this 17 April event will focus on the plasmasphere, but will demonstrate that global imaging provides a unique perspective to study the dynamic evolution of the entire magnetosphere-ionosphere system.

In the following section we provide an overview of the 17 April 2002 event.

2. 17 April 2002 Overview

17 April 2002 was the first day of a strong, four-day-long series of geomagnetic storms. (For more information about the 17-20 April 2002 storms, see *Liemohn et al.* [2004].) Figure 1 gives an overview of 17 April. Figures 1a and 1b show the Kp, Dst and Sym-H indices. Figures 1c through 1g show interplanetary magnetic field (IMF) and solar wind measurements acquired by the Advanced Composition Explorer (ACE) [*Stone et al.*, 1998]. The ACE data have been time-delayed 50 minutes to account for propagation to a nominal 10 $R_{\rm E}$ magnetopause from ACE's upstream location of $(X, Y, Z) = (220, 28, -12)\, R_{\rm E}$. An uncertainty of $\pm$ 7 minutes was obtained for the propagation delay by comparing the timing of ACE data with that of the Wind spacecraft, which was located at $(X, Y, Z) = (12, 190, 90)\, R_{\rm E}$ (in GSM coordinates). ACE magnetic field vectors are plotted in the GSM coordinate system.

On 17 April, a shock in the solar wind (SW) arrived at the magnetopause at approximately 1100 UT. Before 1100 UT, relatively calm and/or steady solar wind and IMF conditions were observed. $B_{\rm z,IMF}$ (Figure 1e) was northward or steady southward (about -10 nT). Solar wind dynamic pressure was low, with solar wind proton density $N_{\rm SW}$ (Figure 1f) below 10 cm^{-3} and solar wind speed $V_{\rm SW}$ (Figure 1g) below 350 km/s. After 1100 UT relatively steady $B_{\rm z,IMF}$ gave way to north-south excursions of amplitude 20 nT or so, and $B_{\rm y,IMF}$ (Figure 1d) changed to strong dawnward ($-Y$). At

1100 UT, the solar wind speed exhibited a step-like transition to 450 km/s, and then ramped up to 600 km/s over the following twelve hours. After 1100 UT the solar wind proton density spiked upward to 70 cm^{-3} and then fluctuated about a mean value of 25 cm^{-3} for several hours. These solar wind conditions are reflected in the Dst, Sym-H, and Kp geomagnetic activity indices (Figures 1a and 1b). The hourly Dst index, a crude indicator of the equatorial magnetic perturbations associated with the stormtime ring current, dropped down to -98 nT (i.e., storm condition) by 17 UT and then gradually began to recover. The 1-minute-resolution Sym-H index exhibited a similar time development. The 3-hour Kp index, which measures mid-latitude magnetic disturbances on a logarithmic scale (from 0–9), showed an increase from 3^- (during the 6–9 UT bin) to 6 (the 9–12 UT bin), coincident with the 1100 UT solar wind transition.

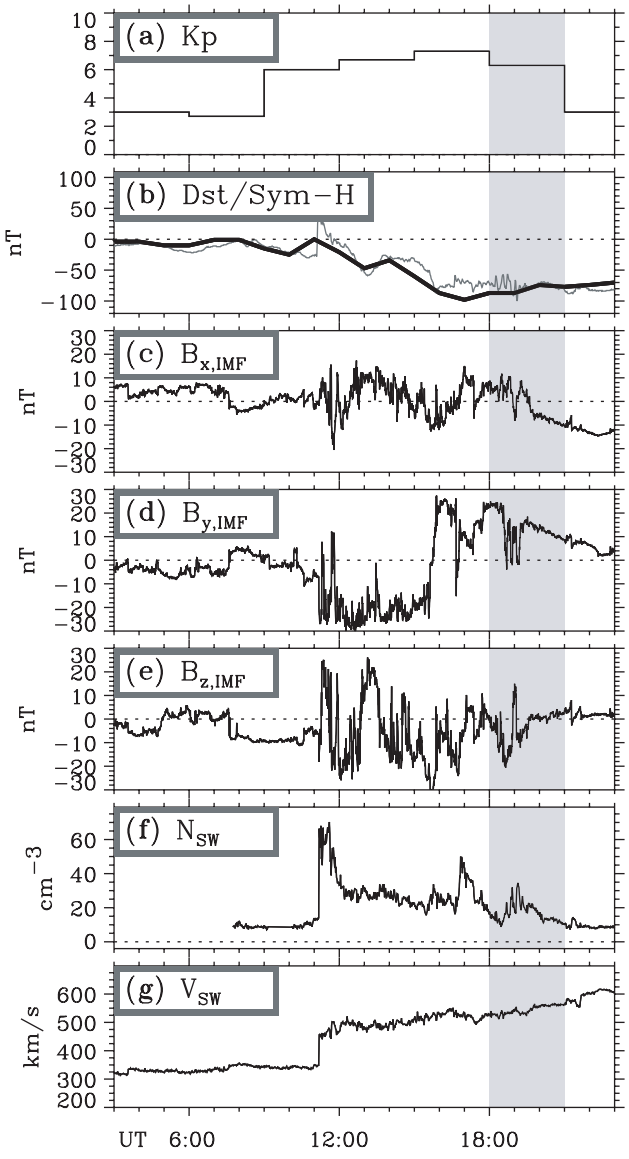

Figure 1. Overview of the 17 April 2002 event. Panels 1a and 1b show the Kp, Dst (thick black) and Sym-H (thin dark gray) indices. Panels 1c through 1g show ACE data: three components (in GSM coordinates) $B_{x,IMF}$, $B_{y,IMF}$, and $B_{z,IMF}$ of the interplanetary magnetic field (IMF), and solar wind (SW) proton density N_{SW} and solar wind speed V_{SW}. The ACE data have been time-delayed 50 minutes to account for propagation to the magnetopause.

The time period of interest in this paper is 1800–2100 UT, indicated by the gray shaded portion of Figure 1. During this period, Kp was 6^+; Dst increased gradually from −87 nT to −75 nT (i.e., storm recovery). The solar wind density was between 10 cm^{-3} and 30 cm^{-3}, and the average solar wind speed was about 550 km/s. $B_{y,IMF}$ was strongly duskward (mostly above 10 nT in the $+Y$-direction) and $B_{z,IMF}$ underwent three rapid polarity changes: southward at 1820 UT, northward at 1856 UT and southward again at 1905 UT. The magnitude of the AE and AU indices (not shown because only browse AE/AU data are currently available for this event), sometimes useful for diagnosing substorm activity, increased dramatically after 1900 UT and peaked at 1930–2000 UT.

In the next sections we will present global views and in situ observations of the coupled response of the plasmasphere, aurora, ring current and ionosphere to these solar wind and IMF conditions. Most of our analysis will focus on the plasmasphere; our examination of the other regions will be mostly limited to how they are coupled to the plasmasphere. Each section will be primarily concerned with a single region, but in many instances we will refer to other sections to discuss aspects of inter-region coupling. In Section 7 we will construct an overall picture based on all the observations presented.

3. Plasmaspheric Dynamics

In this section we discuss plasmasphere dynamics on 17 April 2002, as determined from IMAGE EUV global images.

3.1. Global Plasmapause Location

Since 2000, global images of the plasmasphere have been routinely obtained by the IMAGE extreme ultraviolet (EUV) imager [*Sandel et al.*, 2000, 2001, 2003]. EUV consists of three wide-field (30°) cameras, each tuned to detect 30.4-nm ultraviolet sunlight resonantly scattered by plasmaspheric He^+ ions. Because the plasmasphere is optically thin to 30.4-nm ultraviolet light, the measured brightness of a pixel in an EUV image is proportional to the He^+ column abundance integrated along the line of sight through the plasmasphere. With a 10-minute integration time, EUV images capture the portion of the plasmasphere corresponding to electron densities above $\approx$40 cm^{-3} [*Goldstein et al.*, 2003c; *Moldwin et al.*, 2003]. In this paper we study the motion of global plasmapause curves extracted from EUV images. Plasmapause extraction involves identifying a steep gradient in the EUV He^+ distribution and mapping its location to the equatorial plane using an assumed magnetic (B) field [*Roelof and Skinner*, 2000]. (In this paper we assume a dipole B-field for EUV plasmapause analysis.) Such extracted plasmapause curves have been demonstrated to agree with simultaneous (or nearly-simultaneous) in situ plasmapause-location measurements to within a few tenths of an Earth radius (R_E) [*Goldstein et al.*, 2003c; *Spasojević et al.*, 2003; *Moldwin et al.*, 2003; *Goldstein et al.*, 2004b]. When the plasmapause density gradient is steep and well-defined, EUV plasmapause locations can agree with in situ locations to within one EUV pixel, about 0.1 R_E when images are obtained from orbit apogee.

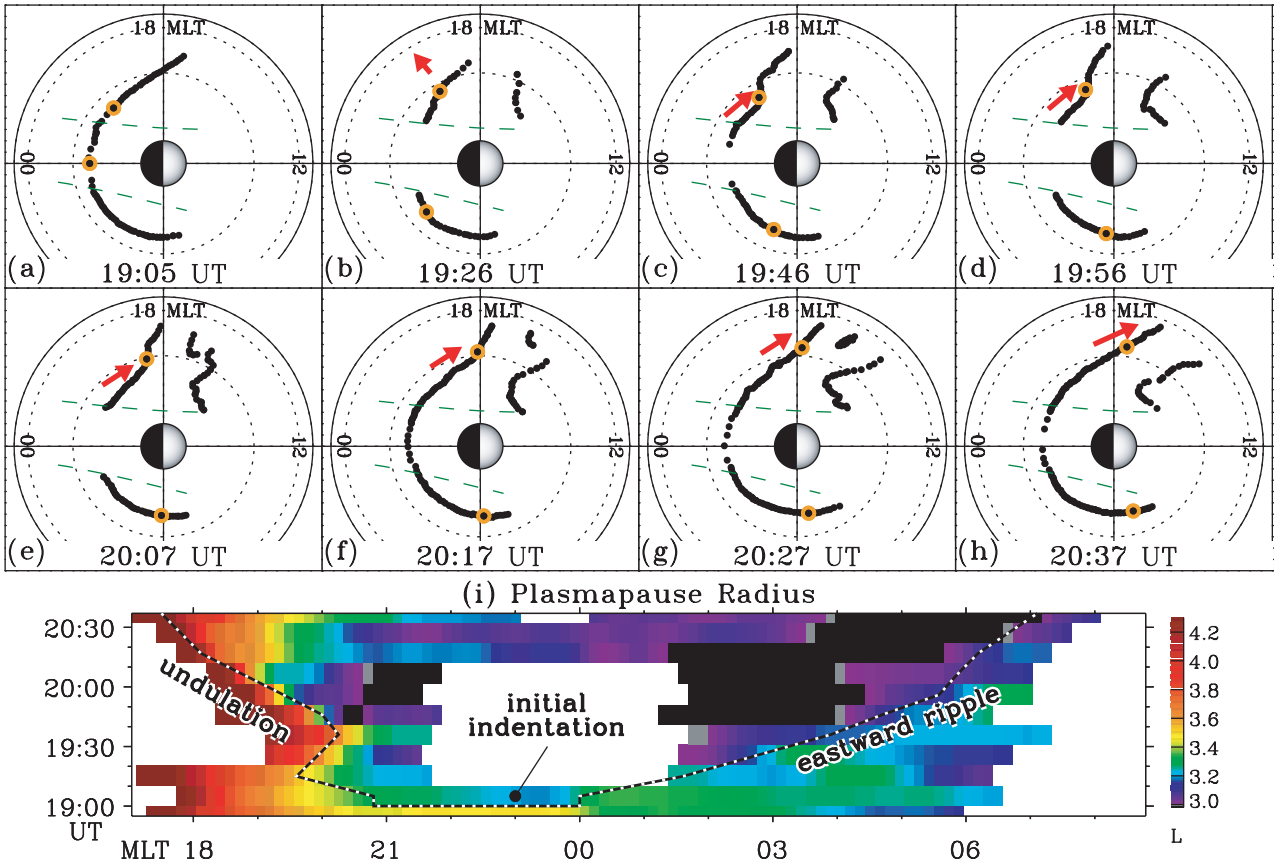

Figure 2. IMAGE EUV plasmapause data from 17 April 2002. Panels 2a through 2h (top two rows) each show a view of the magnetic equatorial plane (in SM coordinates). Dotted circles are at L =4, 6; the solid circle is geosynchronous orbit. The center camera edges are drawn as dashed green lines. The manually-extracted equatorial plasmapause boundary is given by the black dots. The red arrows indicate boundary motion described in the text. Panel 2i (bottom panel) shows a keogram-style plot of plasmapause L (indicated by the color scale) versus MLT and UT. White areas indicate no data. The MLT-UT progress of ripples (see text) is indicated by the dotted line that forms a 'V'-shape. The duskside and dawnside ripple locations are also plotted in Panels 2a through 2h as orange circles.

Figure 2 shows a series of plasmapause shapes extracted from EUV images at eight different times between 1905 UT and 2037 UT on 17 April 2002. The time label in each panel refers to the middle of each 10-minute integration time. Each panel of the top two rows of Figure 2 shows a view of the magnetic equatorial plane (in SM coordinates), with the Sun-direction (i.e., $+X_{SM}$) to the right, and the Earth drawn in the center. For reference, each plot includes magnetic local time (MLT) labels at 1200 MLT (noon), 1800 MLT (dusk), and 0000 MLT (midnight). Gaps in the extracted plasmapause curves are where no plasmapause was identifiable, owing to noise or sunlight contamination, especially in the center EUV camera. For example, in the 1926 UT snapshot of Figure 2b the gap between 2130 MLT and 0130 MLT on the nightside is caused by sunlight contamination in the center camera, which resulted in obscuration of the plasmapause. For reference, the center camera edges are drawn as dashed green lines in each of the equatorial plots of Figure 2. In some cases (e.g., Figures 2c and 2h) sunlight contamination in the center camera resulted in only partial obscuration of the plasmapause. (For more discussion of instrument artifacts on 17 April, see *Goldstein et al.* [2004a].) The plasmapause extraction involves some uncertainty, which we estimate to be about 0.1 R_E on the nightside and dawnside where the plasmapause density gradient is steep, and no more than 0.4 R_E near dusk [*Goldstein et al.*, 2004a]. The extracted plasmapause points of Figure 2 were obtained by manually dragging a computer cursor across the boundary in each of the 17 April EUV images, and so plasmapause points were obtained with point-to-point spatial separation (resolution) that is smaller than the EUV pixel size. As such, the extracted plasmapause may be considered a visual interpolation of the pixelated plasmapause in the EUV image.

The plasmapause curves of Figure 2 suggest a period of erosion before 1905 UT, as follows. Between 1905–2037 UT the nightside and dawnside plasmapause had a smooth, almost circular MLT-shape, with the plasmapause radius at $L \approx 3.3$, except near dusk (west of 2000 MLT) where a larger plasmapause radius accompanied the presence of a drainage plume. Smooth nightside plasmapause shapes and duskside drainage plumes are features typical of the active-time plasmasphere as seen by IMAGE EUV [*Spasojević et al.*, 2003], and reflect disturbed geomagnetic conditions that prevailed after 1100 UT on 17 April.

Figures 2b through 2h illustrate the dynamic evolution of the 17 April duskside 'plasmapause undulation' event reported by *Goldstein et al.* [2004a]. The undulation consisted of two phases. In the first phase (1915 UT to 1936 UT) the pre-midnight plasmapause moved outward, and this outward

motion (depicted in Figure 2b by a red arrow) produced a 0.4–0.5-R_E bulge centered at about 2000 MLT. The origin of this mild bulge is not known, although we will speculate in Sections 3.3 and 5.1. In the second phase (1936 UT to 2037 UT) a large ($\approx 1\,R_E$) indentation formed at the eastern edge of the mild bulge, creating a ripple (i.e., an azimuthal gradient in the plasmapause radius), as shown in Figure 2c. This ripple subsequently propagated westward (i.e., toward dusk, or earlier MLT); the westward progress of the ripple is indicated by the red arrows in the equatorial plots of Figure 2. The formation of the mild initial bulge, and the subsequent formation and westward motion of the indentation/ripple produced a dramatic undulatory motion of the duskside plasmapause. With the passage of the undulatory ripple across the plasmapause, the mild bulge that had formed during 1915–1936 UT was apparently stripped off and pushed westward, as though propelled by a region of enhanced flows with a well-defined inner edge. *Goldstein et al.* [2004a] showed that this region of enhanced flows was the subauroral polarization stream (SAPS), as described further in Sections 3.2.3, 5.2 and 7.

Figure 2i (bottom panel) shows a keogram-style plot of plasmapause L-values versus MLT and UT. Plasmapause L is given by the color scale at the right of the plot. White areas indicate no data. The white strips between 2130 MLT and 0130 MLT are where the plasmapause was obscured by sunlight contamination in the center camera.

The duskside undulation was part of a larger, global plasmapause motion that originated with a slight (0.2–0.3 R_E) indentation of the pre-midnight (2100–2400 MLT) plasmapause between 1855 UT and 1905 UT. In Figure 2i, this initial indentation appears as the 1900 UT, 2100–2400 MLT transition from yellow (L = 3.5) to cyan/green (L =3.2–3.3) that is outlined with the black and white dotted line. At the MLT-edges of this indentation, the plasmapause bulged outward, forming 'ripples.' In Figure 2i the ripples at the edge of the indentation appear as green/yellow pixels west of 2100 MLT and green pixels east of midnight. The ripples are defined as azimuthal gradients in the plasmapause radius. As time progressed these ripples propagated azimuthally, so that the initial indentation widened, expanding both eastward and westward. The ripple MLT-UT locations are indicated in Figure 2i by the black and white dotted lines that originate at the initial 1900 UT indentation, forming a 'V'-shape. The ripple locations (both westward-moving and eastward-moving) are also indicated in each snapshot of Figures 2a through 2h by orange circles.

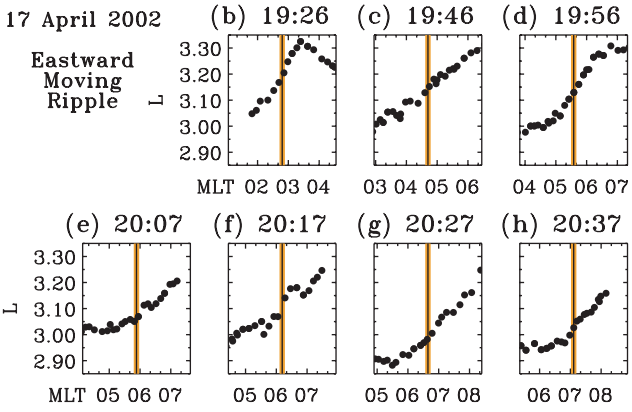

Figure 3. Close-up view of the eastward-moving dawnside ripple. Each panel shows plasmapause L-value versus MLT, spanning 3.5 MLT-hours and centered at the MLT-location of the ripple (vertical line). Compare Panels 3b through 3h with Panels 2b through 2h.

In the pre-midnight sector the ripple's motion changed direction twice, as follows (and indicated by the dotted black and white line). After 1905 UT and until 1915 UT, the ripple moved westward from 2100 MLT to 1930 MLT, at which point the formation of the mild outward-moving pre-SAPS bulge (discussed above, Figure 2b) caused a slight eastward motion of the ripple. After 1936 UT the azimuthal gradient at the eastern edge of the bulge steepened, and the steep ripple commenced moving westward again. In further discussion we shall frequently refer to this pre-midnight ripple as the 'westward-moving' ripple despite the slight eastward motion between 1915 UT and 1936 UT. The motion of the pre-midnight ripple created an undulatory motion of the duskside plasmapause (as discussed above); this westward-moving pre-midnight ripple is labeled 'undulation' in Figure 2i. At the beginning of the undulation event, the plasmapause radius east of (i.e., behind) this traveling undulatory ripple was about 1 R_E smaller than that to the west (i.e., ahead); for example, see the orange dot at 2001 MLT in Figure 2c. Later in the event, the ripple gradient gradually decreased (e.g., Figure 2g).

A smaller (0.2–0.4 R_E) ripple also propagated eastward from the pre-midnight initial indentation, as indicated by the black and white dotted diagonal line labeled 'eastward ripple' in Figure 2i, and by the the eastward-moving orange dot in the equatorial plasmapause plots of Figures 2a through 2h. Although barely detectable in the static snapshots of Figures 2a through 2h, the eastward motion of this small ripple is quite noticeable in an animated sequence of successive EUV images, and is quite clear in Figure 2i. Another view of the eastward-moving ripple is provided in Figure 3. Each panel of Figures 3b through 3h is a close-up of the dawnside portion of the plasmapause shown in the corresponding panels of Figures 2b through 2h. In each panel, plasmapause L value is plotted versus MLT as a series of solid dots. The MLT range of the plot spans 3.5 hours, centered at the MLT location of the moving ripple; the ripple's MLT location is indicated by the vertical line. Behind (west of) the eastward-moving ripple, the plasmapause radius was reduced by 0.2–0.4 R_E relative to the plasmapause radius ahead of (east of) the ripple.

The duskside undulation produced virtually no net displacement of the plasmapause west of about 2000 MLT, as can be seen by visual inspection of the plasmapause curves before the undulation at 1905 UT (Figure 2b), and after the undulation at 2037 UT (Figure 2h). This 'plasmapause L conservation' was mostly due to the fact that although a mild bulge was created when the pre-midnight plasmapause moved outward between 1915 UT and 1936 UT, this mild bulge was subsequently stripped away by westward SAPS flows. Between 2000 MLT and 2300 MLT in Figure 2i, there is also evidence of a slight plasmapause rebound (i.e., outward plasmapause motion) during 2007–2017 UT. This slight rebound (mentioned later in Section 6) was not enough to entirely restore the 2000–2300 MLT plasmapause to its pre-undulation location. East of midnight MLT, where no significant or detectable rebound occurred (as evinced by the black/purple region above the eastward ripple line in Figure 2i), the net inward displacement of the plasmapause between 1905 UT and 2037 UT was about 0.2–0.4 R_E.

Next we present deduction of electric fields from the 17 April 2002 plasmapause motion.

3.2. Electric Field at the Plasmapause

3.2.1. E-field from Plasmapause Motion.

Goldstein et al. [2004c] demonstrated a technique (similar to that of *Carpenter et al.* [1972]) for inferring the electric (E) field associated with the motion of the plasmapause, assuming this boundary motion results from $E \times B$ drift of cold plasmaspheric plasma within or along the boundary. Motion of the plasmapause boundary can result from either (1) compression or rarefaction of the plasmasphere (i.e., plasma moving radially) or (2) erosion of the outer plasmasphere (i.e., azimuthal motion of plasma resulting in the stripping away of the outer plasmasphere). Both these types of general motion can be analyzed to yield associated E-fields. A significant limitation is that it is usually not possible to track the motion of plasma along (i.e., tangent to) the plasmapause boundary, so in general we only have knowledge of the motion perpendicular to the plasmapause, and thus we can only infer the electric field component that is tangent to the boundary.

Following *Goldstein et al.* [2004c], we use the notation $\hat{\pi}$ for the unit vector tangent to the plasmapause and E_π for the corresponding tangential E-field component. Viewed from a vantage point north of the magnetic equatorial plane, the unit vector $\hat{\pi}$ follows the plasmapause curve in the counter-clockwise direction; for a circular plasmapause, $\hat{\pi}$ points eastward. The plasmapause is a dynamic boundary, and in the most general case its shape can be an arbitrary function of radius (r) and azimuth (φ). Therefore, $\hat{\pi}$ evolves with time and does not conform to a standard orthogonal coordinate system. It would be convenient to express E_π in terms of standard coordinates $\hat{r}$ and $\hat{\varphi}$; in general, E_π is composed of contributions from both E_r and E_φ. Rearranging Equations (3) and (6) of *Goldstein et al.* [2004c] (and noting that $E_r \equiv -r\dot{\varphi}B$) allows us to compute the azimuthal E-field E_φ, given E_π and $\dot{\varphi}$:

$$E_\varphi = \frac{E_\pi}{\hat{\pi}\cdot\hat{\varphi}} + \dot{\varphi}\, B \left(\frac{\partial R}{\partial \varphi}\right)_t . \qquad (1)$$

In this relation, $\hat{\pi}$ is the unit vector tangent to the plasmapause, $\hat{\varphi}$ is the azimuthal unit vector, and B is the magnetic field (assumed dipolar). The last term $(\partial R/\partial\varphi)_t$ in Equation (1) is the azimuthal derivative of the plasmapause radius R, and is a measure of the non-circularity of the plasmapause. Note that for a circular plasmapause, this term is zero, and $\hat{\pi}\cdot\hat{\varphi} = 1$. Thus in the special case where the plasmapause is approximately circular, $\hat{\pi} \approx \hat{\varphi}$ and E_π reduces to the conventional azimuthal E-field component E_φ [*Goldstein et al.*, 2004c]. However, for non-circular plasmapause shape, an estimate of the plasma's azimuthal flow speed $\dot{\varphi}$ is required to get E_φ. In the next subsection we will show how the propagating ripple of 17 April 2002 provides such an estimate for $\dot{\varphi}$.

3.2.2. 17 April 2002 Plasmapause E-field.

We applied the *Goldstein et al.* [2004c] technique to obtain an electric field from the extracted plasmapauses of 17 April 2002; the result is shown in Figure 4. In Figure 4a (upper left panel), E_π is presented in keogram format, with E-field plotted versus UT (vertical axis) and MLT (horizontal axis). Color represents the value of E_π (as given by the colorbar). White areas denote where no plasmapause was obtained; sunlight contamination in the center camera shows up as the white strips between 2130 MLT and 0130 MLT. The uncertainty ΔE_π in the value of E_π is approximately 0.4–0.5 mV/m [*Goldstein et al.*, 2004a].

E_π is negative for inward motion of the plasmapause; in Figure 4 inward motion ($E_\pi < 0$) is given by the green-yellow-red portion of the color scale. The V-shaped feature composed of the green-yellow-red pixels is the signature of the indentation and eastward- and westward-traveling ripples (described in the previous section, and depicted in Figure 2i). A traveling ripple shows up as negative E_π (inward motion) because (except for the formation of the mild bulge during 1915 UT to 1936 UT) on 17 April 2002 the ripple marked the leading edge of an expanding indentation of the plasmapause. At a given MLT value, the passage of the ripple left a reduced plasmapause radius in its wake.

Other than the ripple signature, most of the plot is cyan or sky blue ($E_\pi \approx 0$); in other words, the plasmapause motion was almost exclusively confined to the indentation and ripples. There are a few dark blue pixels, especially near dusk between 1915 UT and 2017 UT, indicating outward plasmapause motion ($E_\pi > 0$). The blue pixels at 1915 UT and 1926 UT and centered at 2000 MLT are the signature of the formation of the mild bulge (Figure 2b). The blue pixels at 2007 UT between 2000–2200 MLT are evidence of the pre-midnight plasmapause 'rebound' effect (described near the end of the previous section and in Section 6).

To highlight the initial indentation and propagating ripples of this event, Figure 4b (upper right panel) includes only E_π corresponding to inward motion and with magnitude exceeding the uncertainty ΔE_π; i.e., Figure 4b shows $E_\pi < -0.5$ mV/m only. (In this plot we ignore the positive E_π values during 1915 UT and 1926 UT that correspond to the formation of the mild 2000 MLT bulge; E_π corresponding to the bulge formation will be presented in Figures 4e and 4f, in Section 3.2.4.) The colorbar for Figure 4b is the same as that of Figure 4a. From Figure 4b it can be seen that the earliest indentation occurred at pre-midnight (2100–2400 MLT) between 1855 UT and 1905 UT. As discussed in the previous section, this initial indentation (labeled 'initial' in Figure 4b) then widened, expanding both eastward and westward. The V-shaped signature in Figure 4b marks the locations of the two ripples found at the leading edges of the MLT-expansion of the indentation. The pre-midnight MLT branch of the 'V' is the signature of the westward-propagating sharp indentation that removed the mild 2000 MLT pre-SAPS bulge during the undulation. The post-midnight branch of the 'V' is the signature of the smaller eastward-moving ripple. The SAPS is a radially-localized channel of enhanced westward flow generally located at or just outside the dusk-to-midnight plasmapause. In Sections 3.2.3 and 5.2 we will say more about SAPS.

Indentation of the plasmapause is a motion *normal* to the boundary, allowing us to infer E_π, the component of electric field tangent to the boundary. The presence of a clear ripple signature indicating the progress of this indentation *along* the boundary allows us to very crudely estimate $\dot{\varphi}$. Thus for the 17 April event it will be possible to use Equation (1) to extend the technique of *Goldstein et al.* [2004c] and estimate the total vector electric field at the plasmapause.

In Figure 4b, the initial 1855–1905 UT pre-midnight indentation signature is horizontal between 2100 MLT and 2400 MLT; i.e., this indentation showed no evidence of any

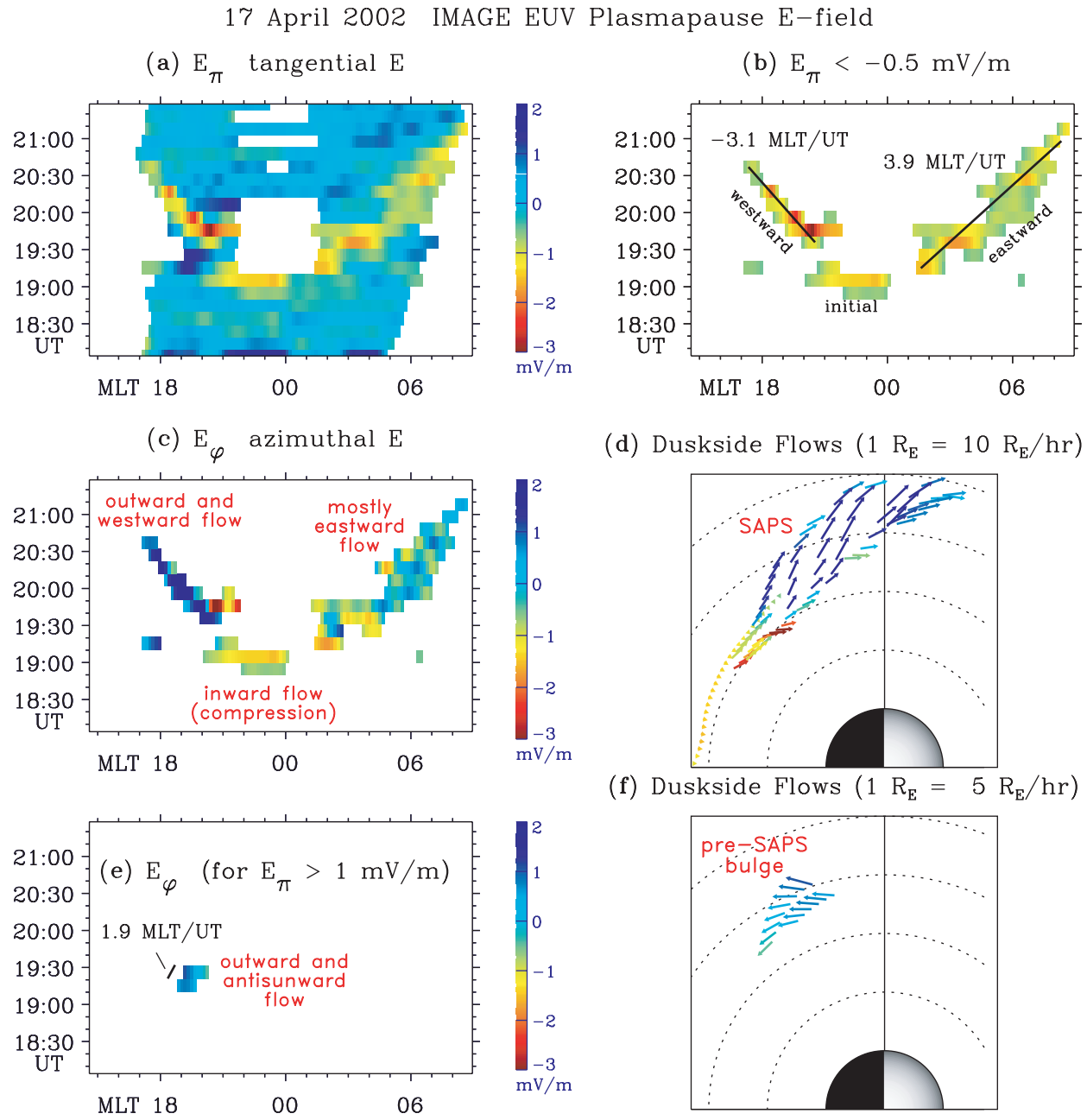

Figure 4. Electric fields deduced from plasmapause motion in IMAGE EUV images, 17 April 2002. Panel 4a (upper left panel): keogram of E_π (given by the colorbar) versus UT and MLT. White areas denote no plasmapause data. Panel 4b includes only $E_\pi < -0.5$ mV/m to highlight the V-shaped signature of the initial indentation and ripples (described in the text). Panel 4c (middle left panel): E_φ. Panel 4d: full vector flow information for the SAPS flow channel (see text). Flow arrows color-coded according to E_φ of Panel 4c. Dotted circles at integer L values. Panel 4e: E_π for the mild pre-SAPS bulge formation (see the text). Panel 4f: vector flows for the bulge formation.

azimuthal motion at the time cadence of EUV images (10 minutes). Of the two possible explanations for this, the first is that azimuthal motion occurred too fast to be temporally resolved by EUV imaging. For this explanation to hold, plasma in the pre-midnight range between 2100 MLT and 2400 MLT would have to move 3 MLT hours in 10 minutes, or about 6 times faster than observed outside this pre-midnight MLT range. While this rapid plasma motion is not impossible, a more likely explanation is that the 2100-2400 MLT pre-midnight sector experienced a nearly simultaneous indentation, i.e., plasma motion was almost entirely radial and $\dot{\varphi} \approx 0$.

In Figure 4b, lines have been drawn on top of the signatures of the eastward- and westward-propagating ripples where global azimuthal motion was detectable as a diagonal signature. West of 2100 MLT the slope of the line is −3.1 MLT/UT, corresponding to azimuthal plasma speed $\dot{\varphi} = -0.8$ radians per hour (rad/hr). East of 0100 MLT the slope of the line is +3.9 MLT/UT, corresponding to azimuthal plasma speed $\dot{\varphi} = 1.0$ rad/hr. Thus, using the observed eastward and westward azimuthal propagation of

the ripples, plus the apparent simultaneous indentation of the 2100-2400 MLT plasmapause, we approximate the azimuthal plasma speed $\dot{\varphi}$ in rad/hr as:

$$\dot{\varphi} = \begin{cases} -0.8 \text{ rad/hr} & \text{if MLT}< 2100 \\ 0.0 \text{ rad/hr} & \text{if } 2100 < \text{MLT} < 2400 \\ 1.0 \text{ rad/hr} & \text{if MLT}> 2400 \end{cases} . \quad (2)$$

This equation is only valid at the time-dependent location of the ripples (i.e., within the 'V'-shaped area of Figure 4b), because it is only the motion of the clearly-identifiable ripples that allows us to approximate $\dot{\varphi}$. Outside the 'V'-signature, we do not have information about azimuthal motion. Note that the observed azimuthal flows at the plasmapause include corotation, so zero $\dot{\varphi}$ implies (or assumes) that the azimuthal component of the non-corotational flow strength exactly balanced that of corotation between 2100 MLT and 2400 MLT. This balancing of corotation inside the 2-MLT-hour pre-midnight sector was probably only approximately correct on 17 April. At MLTs where azimuthal motion was clearly identifiable at the plasmapause, the magnitude of $\dot{\varphi}$ (0.8–1.0 radians/hour, Equation (2)) was approximately three to four times larger than that of corotation (0.26 radians/hour).

Inserting our estimate for $\dot{\varphi}$ into Equation (1) we calculated the azimuthal electric field component E_φ. Figure 4c (middle left panel) displays E_φ in the same format and with the same color scale as the plot of E_π in Figure 4b. Only the portion of E_φ corresponding to the indentation and traveling ripple (excluding the outward motion of the mild bulge formation) is shown because it is only by using the motion of the ripple that we can estimate $\dot{\varphi}$ to obtain E_φ. Note that at the location of a ripple there is an azimuthal gradient in the plasmapause radius, so that E_π can have contributions from both E_φ and E_r.

Near midnight, E_φ is westward (i.e., $E_\varphi < 0$), corresponding to inward radial motion, or a compression of the plasmapause. East of about 0400–0500 MLT, the average E_φ is close to zero, indicating that near dawn the plasma motion implied by the motion of the ripple (as described by Equation (2)) is mostly azimuthal. West of 2000 MLT E_φ is eastward, indicating outward radial motion ($E_\varphi > 0$) added to the westward azimuthal motion ($E_r > 0$) of the ripple (Equation (2)). Thus, at dawn and dusk E_φ is drastically different from the corresponding values of E_π, illustrating that there can be a significant difference between the motion of the boundary, and the motion of the plasma that lies just inside that boundary. Near dusk, the boundary moved inward by about 1 R_E, but our analysis suggests the plasma was moving both westward and outward, so that the inward plasmapause motion was due to erosional motion, a stripping away of the outer plasma layer. Our analysis demonstrates that electric fields inferred from plasmapause boundary motion can be used to analyze both compressional (radial) and erosional (azimuthal) plasma motions.

3.2.3. SAPS Flow Channel.

Using E_φ (Figure 4c) and $E_r = -r\ \dot{\varphi} B$ (calculated using $\dot{\varphi}$ from Equation (2)), we estimated the total electric field, which we represent in terms of flows. Figure 4d shows flow vectors on the duskside (i.e., west of midnight MLT). The flow vectors are scaled so that 1 R_E of length equals 10 R_E/hour flow speed. For easy comparison with Figure 4c (useful for assigning UT values to arrows), the vectors are color-coded according to E_φ value.

Between 2100 MLT and 2400 MLT Figure 4d shows pure compression (flows pointing inward, pure westward E_φ), as mandated by our assumption of zero $\dot{\varphi}$ in that MLT sector (Equation (2)). West of about 2040 MLT, flow vectors are oriented roughly along the path the duskside undulation took as it traveled westward along the plasmapause. These duskside flow vectors (colored blue in Figure 4d) seem to define a distinct flow channel, which supports the interpretation (Section 3.1) that the undulatory ripple was caused by a flow channel that pushed plasma westward along the plasmapause, stripping away the outer plasmasphere layer. *Goldstein et al.* [2004a] showed that the 17 April duskside flow channel implied by Figure 4d was most likely caused by the subauroral polarization stream (SAPS). [*Foster et al.*, 2002; *Anderson et al.*, 2001]. On average, the SAPS effect is concentrated most strongly in the dusk-to-pre-midnight MLT sector, and produces in the equatorial plane a radially-confined channel of flows that are both westward and radially outward. The SAPS flow channel is usually 1–2 R_E in radial extent, with a sharp inner edge located at or near the plasmapause. The average shape of the SAPS flow channel found by *Foster and Vo* [2002] has a radial location that gradually increases as MLT decreases between midnight and dusk. All of these average SAPS characteristics are entirely consistent with the EUV-derived duskside flow distribution contained within the region of blue arrows in Figure 4d.

The speed within the EUV-deduced flow region is also consistent with a SAPS interpretation. Near 1800 MLT (and corresponding to about 2017 UT), the flow arrows are about 0.5 R_E long. According to the scale in Figure 4d, this arrow length means a flow speed of about 5 R_E/hour. Mapping this speed to the ionosphere (at 850 km altitude) using an $R^{3/2}$ (magnetic dipole) velocity dependence yields a flow speed of 1.2 km/s, which is comparable to average SAPS flows. In Section 5.2 we will show that the EUV-derived flow speed of 1.2 km/s (at 850 km altitude) is consistent with nearly simultaneous ionospheric in situ data obtained by DMSP.

When the SAPS flow channel overlaps the plasmasphere, it can move the duskside plasmapause inward, stripping off the outermost layer [*Goldstein et al.*, 2003b, 2004b]. The 17 April EUV observations (of the second phase of the undulation) are the first to capture this process, showing how SAPS flows encountered the outer edge of the duskside plasmasphere at about 2015 MLT and 1936 UT, and over the following hour removed a layer of plasma about 1 R_E thick. In Sections 3.2.4, 3.3, and 5.1 we discuss the first phase of the undulation, the pre-SAPS mild bulge formation.

3.2.4. Formation of the Mild Pre-SAPS Bulge.

In this section we shall briefly show electric field analysis from the first phase of the 17 April 2002 plasmapause undulation, the formation of the mild bulge (at about 2000 MLT) that occurred between 1915 UT and 1936 UT.

In Figure 4e is a 2D keogram-style plot of E_φ for the bulge formation. This plot was created as follows. First, pixels from Figure 4a corresponding only to the bulge formation were selected by choosing $E_\pi > 1$ mV/m before 1936 UT. This restriction selected only the dark blue pixel regions near 2000 MLT, at 1915 UT and 1926 UT in Figure 4a. These dark blue pixels define a diagonal line segment with slope +1.9 MLT/UT, or $\dot{\varphi} = +0.5$ rad/hr. In other words, the EUV data imply that during the bulge formation there was a slight eastward motion of plasma. Using this estimate for $\dot{\varphi}$ in Equation (1), the selected E_π pixels were converted to E_φ. It should be noted that this estimate for $\dot{\varphi}$ during the

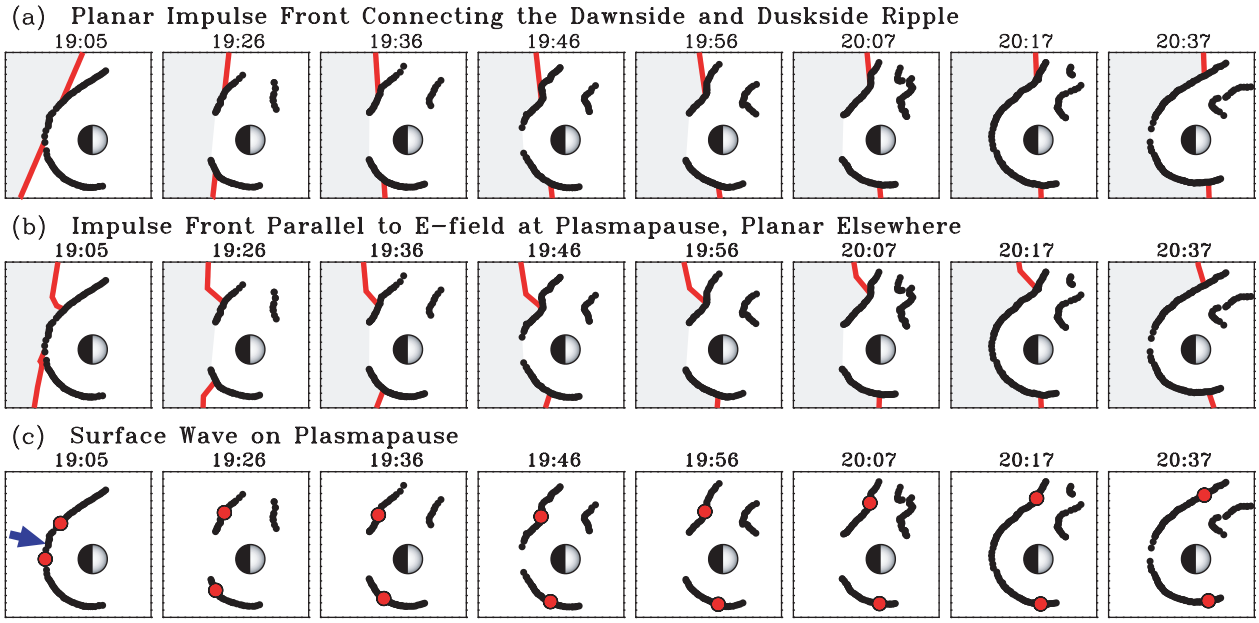

Figure 5. Interpretation of the plasmapause indentation and ripples as a sunward-propagating impulse front, or as surface waves on the plasmapause. Each panel: equatorial shapshot of the plasmapause at a given time (UT value at top of panel). Panel 5a (TOP ROW): thick red line gives planar front obtained from a straight line connecting the dawn and dusk ripple locations (from Figure 2). Panel 5b (MIDDLE ROW): front direction is parallel to the EUV-inferred E-field within 1 R_E of the plasmapause, planar elsewhere. Panel 5c (BOTTOM ROW): two red dots indicate time-dependent locations of traveling surface waves.

pre-SAPS bulge formation has higher uncertainty than the estimate for $\dot{\varphi}$ based on the ripple motion (Equation (2)). The eastward- and westward-propagating ripples depicted in Figure 4b clearly indicate the MLT-UT progress of a distinct feature that can be reliably tracked from one UT to the next. Although the eastward-moving E_π signature of the bulge formation suggests an eastward motion of plasma, it is possible that the plasma motion itself was not eastward. However, in Section 4 we show that during the bulge formation there was a simultaneous eastward motion of an auroral precipitation region (see Figure 7), which offers some support to our interpretation of the bulge E_π signature.

Using E_φ from Figure 4e and using $\dot{\varphi} = 0.5$ rad/hr to estimate E_r, total E-field vectors were calculated, as shown in Figure 4f. The flows inferred from the pre-SAPS bulge formation imply that the plasma moved antisunward at a speed of about 2.5 R_E/hr. In Sections 3.3 and 5.1 we will suggest two possible causes of the bulge formation.

3.3. 'Impulse Front' Interpretation of Ripples

In this section we briefly offer a physical interpretation of the motion of the ripples along the plasmapause. On 17 April the nightside plasmapause indentation was initially (at 1905 UT) localized to a few MLT hours in the pre-midnight sector. During the following 90 minutes the indentation widened to encompass all of the plasmapause between dusk and dawn. Ignoring the formation of the pre-SAPS mild bulge (which we discuss later), we speculate that the global plasmapause indentation arose from a sunward convective impulse that took a finite time to propagate sunward from the magnetotail. In Section 4 we discuss the assertion that this sunward convective impulse was caused by dipolarization of the nightside geomagnetic field during a 1900 UT substorm onset. One interpretation is that the ripples on the dusk- and dawnsides were the intersection of the leading edge ('front') of this impulse with the plasmapause. Given only the plasmapause ripple locations, it is not possible to determine conclusively the global shape of such an impulse front, but we can guess.

At any given time, there were two plasmapause ripples, one at dawn, one at dusk, shown by the pairs of dawnside/duskside orange circles plotted in each of the equatorial plots of Figures 2a through 2h. In the simplest approximation, these two points are joined with a line, and the impulse front is planar. This scenario is depicted in Figure 5a. Each panel shows an equatorial shapshot of the plasmapause at a given time, which is indicated at the top of the panel. The thick red line gives the planar front obtained by connecting the dawn and dusk ripple locations (from Figure 2) at that time. According to the fronts in Figure 5a, the sunward impulse first encountered the nightside plasmapause at an oblique angle, but then turned so that it propagated roughly in the $+X$ direction. An initial approach from pre-midnight is consistent with the idea that the impulse was triggered at least in part by a substorm dipolarization (Section 4), which typically occurs at pre-midnight, judging from the observed behavior of plasma particles injected into the inner magnetosphere by the substorm [*McIlwain*, 1974; *Vagina et al.*, 1996]. From the X locations of the ripples before 1930 UT, they moved approximately 1.25 R_E in the $+X$ direction in 37 minutes, a sunward speed of 3.6 km/s. *Reeves et al.* [1996] found that the earthward propagation speed of the substorm convection front (produced by induced E-fields associated with the substorm dipolarization) was about 24 km/s at geosynchronous orbit ($L = 6.62$ in a dipole field). Assuming $V \propto L^3$, the geosynchronous injection speed 24 km/s corresponds to 3.8 km/s at $L = 3.5$, the approximate location of the pre-midnight plasmapause during the initial indentation. Thus the speed and the angle of approach of the

impulse are both consistent with prior observations of the effects of substorm dipolarizations. It is therefore likely that the 1900 UT substorm onset (Section 4) did indeed initiate the event.

It is worth commenting on the relative speeds of the ripples on the dusk and dawn sides. From a simple picture of the inner magnetospheric E-field, we expect dawnside flows to be faster than duskside flows, because on the dawnside sunward convection adds to corotation, while near dusk convection and corotation oppose each other. From the panels of Figure 5a we see that from 1905 UT to 1936 UT the dawnside ripple did indeed move faster, consistent with the simple picture. However, after 1936 UT the two ripples moved at about the same speed; this duskside flow speed enhancement can be attributed to the presence of the SAPS flow channel that formed about 1930 UT (Sections 3.2.3 and 5.2). Thus proper understanding of duskside plasmasphere dynamics requires inclusion of SAPS [*Goldstein et al.*, 2003b, 2004b, a].

The impulse front divides the inner magnetosphere into two regions, ahead of and behind the front. Behind the impulse front (i.e., to the left of the red line) the plasmapause radius is reduced relative to that in the region ahead of the impulse front (to the right of the red line). As an example, consider the snapshot at 1946 UT. On the duskside the impulse front marks a very clear boundary between smaller plasmapause radius behind the front, and larger radius ahead of the front. On the dawnside the difference is not as great, with only a slight change in plasmapause radius; nonetheless, there is a visible distortion (a flattening) of the plasmapause to the left of the front.

Although the simple planar fronts of Figure 5a are useful for visualization, one problem is that the fronts are not perpendicular to the flows inferred from the plasmapause motion. For example, from Figure 4d the duskside flows were both outward (radial) and westward (azimuthal) after 1936 UT. However, the front direction after 1936 UT is roughly parallel to the Y-axis, implying flows that are purely in the $+X$-direction, inconsistent with the derived duskside plasmapause flows. A perhaps more realistic assumption is that the front of the impulse was diverted around the nightside plasmapause, and that near the plasmapause the front was oriented parallel to the total electric field we inferred from the plasmapause motion. Figure 5b depicts this second scenario. In each panel the front is divided into two regimes. Within 1 R_E of the plasmapause the front is drawn parallel to E, in effect representing a 1-R_E-thick layer of flows that are diverted around the plasmapause. Outside this 1-R_E layer, the front is assumed planar. Although the orientation of the planar front outside the 1-R_E layer is purely speculative, the distortion of the front shape near the plasmapause is probably realistic in a zero-order sense. Because the plasmasphere is much more dense than the surrounding plasma, the sunward convective impulse should be expected to flow around the plasmapause, which acts as a barrier. The SAPS flow channel adds to the distortion near dusk.

Although we cannot be certain of the global shape of the fronts, Figure 5 provides a means of visualizing the global evolution of the plasmapause when a convection increase propagates sunward at a finite speed. As the front proceeds sunward, the global plasmapause radius is reduced in its wake.

There is some observational evidence that the electromagnetic effects of substorm dipolarizations are restricted in local time [*Singer et al.*, 1985; *Erickson et al.*, 2000], and not able to produce a broad impulse that encompasses the entire night side. However, these studies do not definitively rule out the impulse front interpretation for the 17 April event. *Singer et al.* [1985] performed a case study of substorm-related magnetic signals in a limited sample space of L and MLT, and much of the action of the 17 April 2002 event occurred outside this (L, MLT) range. Limited coverage is a well-known problem common to any finite number of single-point measurements, and is a problem that global imaging was designed to address. The synoptic study of *Erickson et al.* [2000] achieved much more extensive coverage, but while valuable, such statistical results cannot hope to capture all of the nuances of the very dynamic physics involved in substorms. In light of these possible objections to the impulse front interpretation, it is worth mentioning an alternate interpretation, that the plasmapause ripples were in fact due to surface waves on the plasmapause, and not caused by a larger global impulse. In this alternate scenario, the initial 2100-2400 MLT indentation was caused by a sunward impulse, and then this indentation widened as surface waves (ripples) propagated eastward and westward. This scenario is depicted in Figure 5c; the initial pre-midnight impulse (indicated by the blue arrow) is converted into purely plasmaspheric motion in the form of two traveling surface waves (each indicated by a red dot). The weakness of this interpretation is that the motion of the eastward- and westward-moving ripples was accompanied by similar motion of precipitation regions (see next section, and Figure 7), and the westward motion of the duskside ripple was accompanied by westward motion of the ring current (see Section 5.1 and Figure 8). If the plasmapause ripples were indeed solely caused by surface waves, the motion of auroral precipitation sites would not be so closely correlated. Thus, while it is possible that surface waves played some small role in the ripple propagation, it is clear that plasmapause surface waves alone cannot account for all the motions of the inner magnetosphere.

Now we discuss the pre-SAPS mild bulge formation during 1915–1936 UT. The impulse front interpretation implies that the plasmapause behind the front was moved inward, but the plasmapause ahead of the front was unchanged. However, there is evidence in Figure 5 that the duskside plasmapause radius was moved outward ahead of the front. For examples, see the 1926 UT plasmapause (which shows the pre-SAPS bulge), and 1956 UT. One possible explanation is that plasma removed from the nightside by the sunward-moving front was diverted around and outside the plasmapause at more sunward locations, an effect similar to the pile-up of snow ahead of a snowplow; as the snowplow advances, the height of the snow ahead of the plow blade increases. This 'snowplow' interpretation is complicated by consideration of the antisunward plasma motion inferred from the signature of the formation of the pre-SAPS bulge. However, as discussed, interpretation of the azimuthal motion during the pre-SAPS bulge formation was more ambiguous than that of the traveling ripples. In Section 5.1 we offer a second possible explanation for the pre-SAPS bulge formation.

4. Auroral Dynamics

In this section we investigate the auroral dynamics of 17 April 2002. We will show details that further support

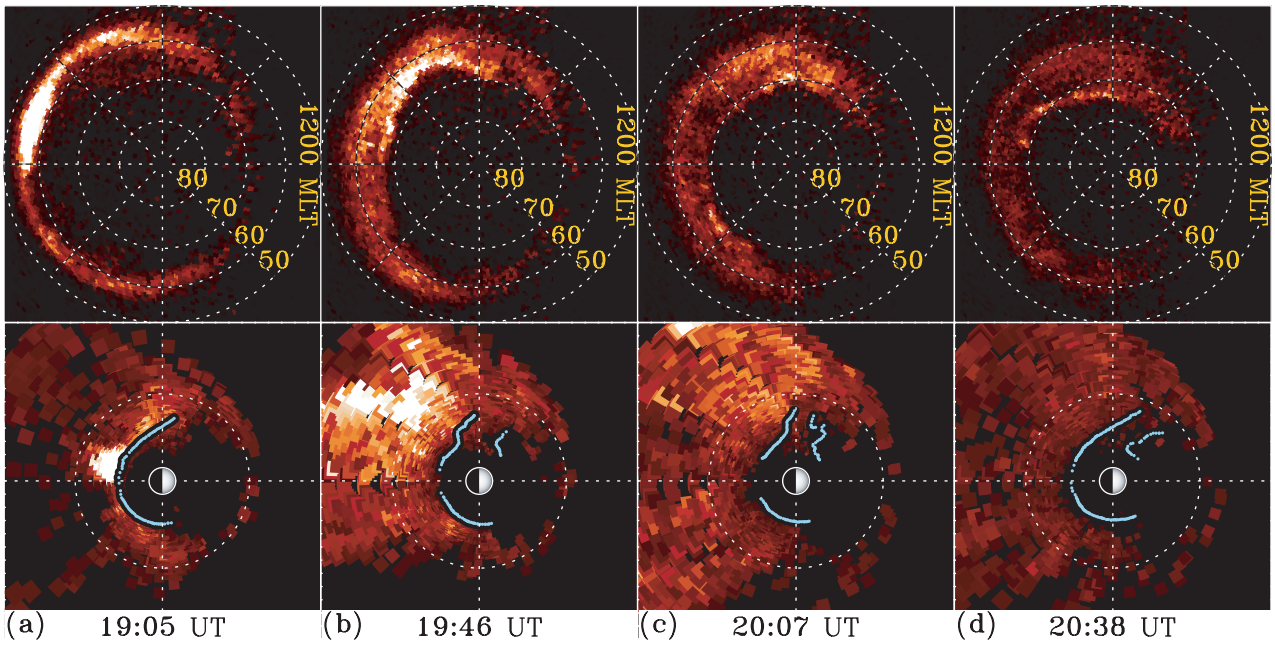

Figure 6. IMAGE FUV measurements of the substorm of 1900–2038 UT on 17 April 2002. TOP ROW: four FUV polar-projection electron aurora images. Circles drawn at 50, 60, 70, 80 degrees magnetic latitude; Lines = magnetic local time. Sun-direction (1200 MLT) to the right, dusk at the top, dawn at the bottom, and midnight to the left. The color is proportional to brightness of the detected auroral emissions. BOTTOM ROW: the same FUV auroral data, mapped to the magnetic equator using the Tsyganenko magnetic field model [*Tsyganenko*, 2002a, b]. Dotted circle = geosynchronous orbit. The EUV-determined plasmapause is overlaid on the mapped auroral images.

the assertion of *Goldstein et al.* [2004a] (mentioned in Section 3.3) that an auroral substorm onset and its associated sunward convective impulse was the major trigger for the 17 April plasmasphere indentation/undulation (described in Section 3).

The SI13 camera of the IMAGE far ultraviolet (FUV) imager obtains global pictures of the electron aurora in 135.6-nm light [*Mende et al.*, 2000]. The top row of Figure 6 contains four FUV images of electron aurora. Each image is a polar projection, plotted versus magnetic latitude (circles) and magnetic local time (lines). In each panel, the Sun-direction (1200 MLT) is to the right, dusk is at the top, dawn at the bottom, and midnight to the left. For reference, 50, 60, 70 and 80 degrees magnetic latitude are labeled. The color is proportional to brightness of the detected auroral emissions. (In our analysis the actual brightness values are irrelevant, although the same normalization is used for all the FUV images.) A background subtraction has been performed to remove a minor amount of sunlight contamination that would otherwise be visible on the dayside below 60° magnetic latitude.

The bottom row of Figure 6 contains the same FUV auroral data, mapped to the magnetic equatorial plane using the Tsyganenko magnetic field model [*Tsyganenko*, 2002a, b]. Overlaid on the mapped auroral images, the EUV-determined plasmapause (from Figure 2) is drawn. The time stamp for each auroral image is indicated at the bottom. Because the EUV image cadence is slower than that of FUV, the EUV plasmapause was taken from the EUV time stamp closest to that listed at the bottom of the plot. The mapped FUV auroral images offer a visually interesting alternate view of the usual polar-projected images, and indicate how distorted from a dipole the geomagnetic field can potentially be. Note that the sunward boundary of the mapped auroral images has a shape similar to what we would expect for the dayside magnetopause, but this shape may reflect the Tsyganenko field model's estimate for the magnetopause rather than a real auroral boundary.

Figure 6a shows the FUV image shortly after the 1900 UT onset of an auroral substorm. In Figure 6a the onset signature is the intense brightening found in the pre-midnight 2100–2400 MLT sector. It is remarkable that the onset occurred in the same MLT range, and at the same time (within the limits of uncertainty of EUV image timing), as the initial plasmapause indentation. Examining the equatorial FUV image, it is also evident that the onset happened at L-values just outside the plasmapause. One should not expect the Tsyganenko model field to exactly capture the magnetic field during times of substorm dipolarization, and it is quite likely that the onset signature belongs on higher L than depicted in Figure 6a, which would be more consistent with the typical $X = -4.3\,R_E$ to $X = -15\,R_E$ range of substorm injections [*Friedel et al.*, 1996]. Nonetheless, the location of the onset signature is very suggestive that it is strongly linked to the initial plasmapause indentation.

In Figures 6b through 6d, later FUV images show that the auroral signature propagated westward and poleward (outward in the equatorial plane), and its intensity dropped. From the equatorial plots (bottom row) it can be seen that the rate of change of the MLT location of the auroral signature agreed with the rate of propagation of the duskside plasmapause ripple. By 2038 UT the ripple had propagated to pre-dusk MLT, and the auroral substorm signature had mostly dissipated.

To further demonstrate the connection between the substorm and the plasmapause indentation/ripples, Figure 7

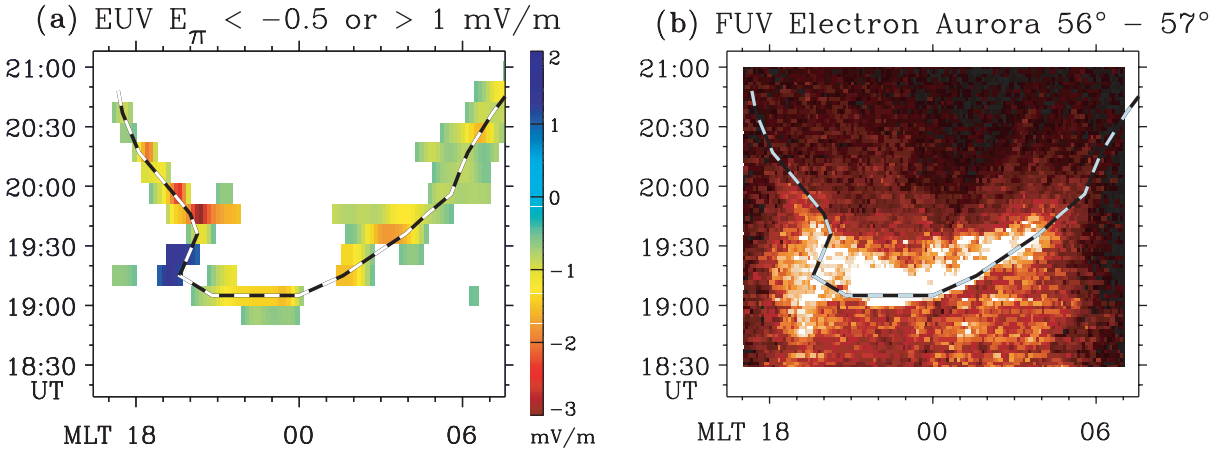

Figure 7. IMAGE EUV electric field E_π and IMAGE FUV SI13 auroral intensities. Thick dashed lines plot the plasmapause ripple locations. LEFT SIDE (Panel 7a): E_π for the traveling plasmapause ripples. RIGHT SIDE (Panel 7b): FUV intensity keogram of the same MLT-UT range as Panel 7a, and from magnetic latitude 56°–57°, showing close correlation between plasmapause and auroral motion.

shows side-by-side plots of the EUV electric field E_π and the FUV intensity. Figure 7a (left side) is a composite of Figure 4b and the E_π signature of the pre-SAPS bulge, highlighting the global 'V'-shaped signature of the traveling dusk- and dawnside ripples. E_π is plotted versus UT and MLT, using the same color scale as that of Figure 4. The thick black/white dashed lines plot the ripple locations as given by the dotted V-shaped lines of Figure 2i. Figure 7b (right side) is a keogram of FUV intensity plotted with the same MLT-UT range as the EUV E_π data. Each pixel is the average FUV intensity in the magnetic latitude range 56°–57°. This latitude range corresponds to L-values just outside the plasmapause. On top of the FUV keogram, the dashed lines give the ripple locations as in Figure 7a. Note that the earliest appearance of the substorm onset is at 1900 UT.

It is remarkable how closely the [MLT, UT] locations of the substorm signature follow the 'V'-shaped signature of the eastward-moving and westward-moving plasmapause indentation ripples. There is close correspondence between the auroral substorm, and the global plasmapause indentation that spread to the entire nightside on 17 April. This correspondence provides strong circumstantial evidence that the substorm onset triggered the convection enhancement responsible for the entire event. Prior to substorm onsets, the geomagnetic field in the tail region of the magnetosphere is stretched as energy is stored in the tail. Substorm onsets are thought to dissipate this energy by reconfiguring the global tail magnetic field from stretched to dipolar geometry [*Ohtani et al.*, 1992]. This dipolarization involves a sunward surge of tail plasma as the stretched field lines become less stretched. Therefore, we argue that a substorm dipolarization at 1900 UT was the main source of the sunward convective impulse depicted in Section 3.3. The excellent agreement between the FUV-observed substorm brightness signature and the EUV-observed ripple locations may indicate that some of the motion of auroral features during substorms is related to the sunward magnetic field motion itself; i.e., auroral precipitation may be intensified at the sunward-moving location of the dipolarization front.

There is an almost vertical signature that reflects a slightly eastward-propagating auroral feature between 1900 MLT and 2000 MLT that preceded the substorm (starting at 1845 UT) and persisted until about 1930 UT. In Figure 7b the portion of this auroral signature after 1915 UT matches up with the MLT/UT signature of the formation of the pre-SAPS bulge, i.e., the blue pixels of Figure 7a. This apparent correspondence between the aurora and the pre-SAPS bulge formation implies that the bulge may have formed via a process involving the plasma sheet/ring current, and also supports the interpretation of Section 3.2.4 that the bulge formed due to an eastward (i.e., antisunward) motion. We will return to this point in the next section.

5. Dynamics of the Ring Current and Subauroral Ionosphere

In this section we show how the ring current responded to the auroral substorm impulse, and how the ring current and ionosphere were together involved in the creation of the SAPS electric field and flow channel that dominated the duskside plasmaspheric dynamics after 1930 UT. We also speculate on the role of the ring current pressure in the formation of the mild duskside bulge that preceded the formation of the SAPS flow channel.

5.1. Global Ring Current Pressure

The IMAGE high-energy neutral atom (HENA) imager [*Mitchell et al.*, 2000] obtains images of the neutral atoms produced by charge-exchange between energetic ions and cold neutral atoms in the Earth's exosphere [*Roelof*, 1987; *Henderson et al.*, 1997]. Thus an ENA image is a convolution of the neutral atom population and the energetic ion distribution. Ion distributions are retrieved from the ENA images using the constrained linear inversion technique described by *Demajistre et al.* [2004] and *C:son Brandt et al.* [2002], and validated by *Vallat et al.* [2004]. The HENA instrument can distinguish between hydrogen and oxygen ENAs; we present equatorial proton pressure distributions only.

Figures 8a through 8e show HENA proton ring current (RC) pressure in the energy range 10–60 keV at five selected times during the 17 April 2002 event. The pressures are color-coded according to the logarithmic scale at the bottom of the figure. For reference, a dashed contour line at 0.54 nPa (or $\log_{10} P = -0.27$), and a thick contour line at 0.8 nPa ($\log_{10} P = -0.1$ have been drawn on top of the color distribution. The dashed contour outlines the ring current

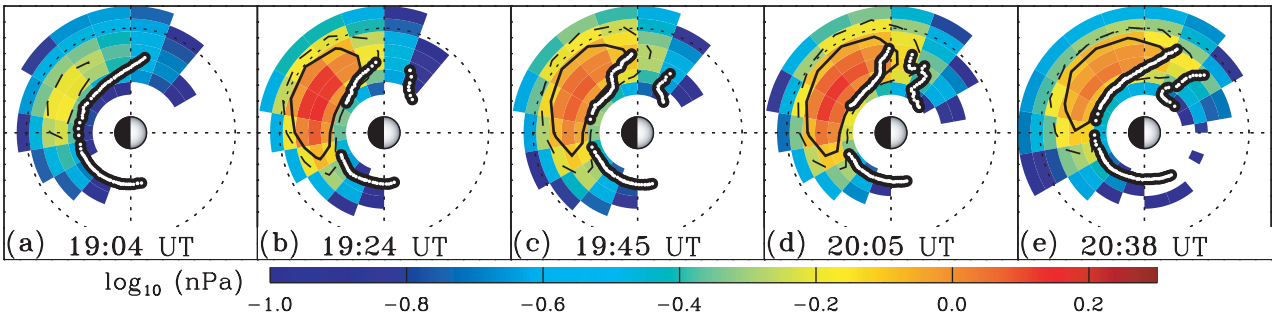

Figure 8. HENA proton ring current (RC) pressure in the energy range 10–60 keV at five selected times on 17 April 2002. Logarithmic colorbar gives proton pressure, with contour lines at 0.54 nPa (dashed) and 0.8 nPa (thick solid line) drawn in. The Sun to the right; dotted circle is geosynchronous orbit. The EUV plasmapause from the nearest-in-time EUV image is overplotted.

injection pressure just after the 1900 UT substorm onset; the solid contour outlines the enhancement of the ring current pressure above this dashed contour. The Sun is to the right, the Earth at the center; the dotted circle is geosynchronous orbit. The EUV plasmapause from the nearest-in-time EUV image is overplotted on each HENA pressure distribution.

At 1856 UT (prior to the substorm onset, not shown), the peak HENA ring current pressure was 0.5 nPa. As shown in Figure 8a, at 1904 UT the 1900 UT substorm onset injection produced a pre-midnight peak in the ring current pressure. The peak pressure after the injection was 0.7 nPa at 1904 UT, and by 1916 UT it had reached 1.1 nPa, double its pre-substorm value. At later times (1924–2038 UT) the ring current peak propagated westward.

Figure 8 shows that on 17 April, the ring current and plasmasphere were almost spatially complementary. From the 1904 UT (Figure 8a), the injection happened in very nearly the same 2100-to-2400 MLT range as the initial plasmapause indentation. At 1924 UT (Figure 8b) the partial ring current with pressure above 0.8 nPa (inside the thick contour line, orange on the color scale) occupied the sector between 1930 MLT and 0200 MLT, roughly the same MLT-extent as the plasmapause indentation at that time (see Figure 2i). There was, however, some overlap between the western edge of the partial ring current and the duskside plasmasphere. At subsequent times the ring current peak propagated westward at the same rate as the duskside undulation, and the leading edge of the $P > 0.8$ nPa ring current was located at about the same MLT as the 1-R_E duskside undulation ripple. The overlap of the partial ring current and the duskside plasmasphere became more pronounced at later times (e.g., see 2038 UT, Figure 8e).

The role of the ring current in the 17 April plasmaspheric dynamics varied with time, from passive at the start of the event to active near the end. Between 1900 UT and 1930 UT, both ring current and plasmasphere reacted to the substorm onset. The sunward flows induced by the dipolarization caused the pre-midnight ring current injection and the pre-midnight plasmapause indentation. After 1930 UT the enhanced ring current pressure gradients provided a suitable location for strong region 2 currents, which linked to the region 1 auroral currents via poleward Pedersen currents in the ionosphere, creating the SAPS electric field (discussed in Section 5.2). This SAPS E-field then modified the duskside plasmasphere density distribution by stripping away the outer 1 R_E layer of cold plasma and moving it westward. Thus, after 1930 UT the ring current dynamics involved coupling with the auroral and subauroral ionosphere, and the ring current played an active role in creating the SAPS that dominated the post-1930 UT duskside plasmasphere dynamics.

There is some indirect evidence that the ring current played an active role in creating the pre-SAPS bulge as well. At 1924 UT (Figure 8b) the HENA ring current peak pressure of 1.4 nPa was located at $L \approx 4.4$ and between 2100 MLT and 2300 MLT. Enhancements in the partial ring current pressure are known to decrease the local geomagnetic field. *Tsyganenko* [2002a, b] showed that during strong storms (Dst< -120 nT) the duskside equatorial geomagnetic field in the vicinity of the ring current could be depressed by -225 nT from a dipole field. For the period 1800 UT to 2100 UT on 17 April, the average Dst was about -80 nT, suggesting a possible magnetic field depression of -150 nT at the location of the peak in the partial ring current pressure. Assuming a -150 nT magnetic field depression occurred between 1900 UT and 1915 UT (i.e., during the initial ring current injection), and taking the width of the ring current to be about 2 R_E (Figure 8b), the time-varying magnetic field (-150 nT/15 minutes) could induce a dusk-to-dawn electric field of about 2 mV/m. From the blue pixels at 19115 UT and 1926 UT in Figure 4a, the electric field (E_π) strength inferred from EUV images during the mild bulge formation was 1 to 2 mV/m. This very crude calculation suggests that reduction of the duskside geomagnetic field strength by the ring current could plausibly have induced antisunward plasma motion that in turn created the pre-SAPS bulge during 1915 UT to 1936 UT. Said another way, it is possible that in the vicinity of the enhanced ring current pressure, the geomagnetic field lines were 'inflated' and this inflation effect caused an antisunward motion of the cold plasmaspheric plasma, creating the bulge. From Figure 7b, the auroral ionosphere may have been coupled to this ring current pressure build-up in some way. The most likely link is the substorm dipolarization itself, which produced both the auroral signature and the ring current pressure increase. The details of the substorm's ring-current-and-aurora coupling are beyond the scope of this paper. This proposed effect, in which magnetic field reduction causes local antisunward convection in the vicinity of the ring current injection, deserves more investigation.

5.2. SAPS in the Subauroral Ionosphere

The Defense Meteorological Satellite Program (DMSP) [*Rich and Hairston*, 1994] obtains in situ data in the subauroral ionosphere at 850 km altitude. The DMSP SSJ4

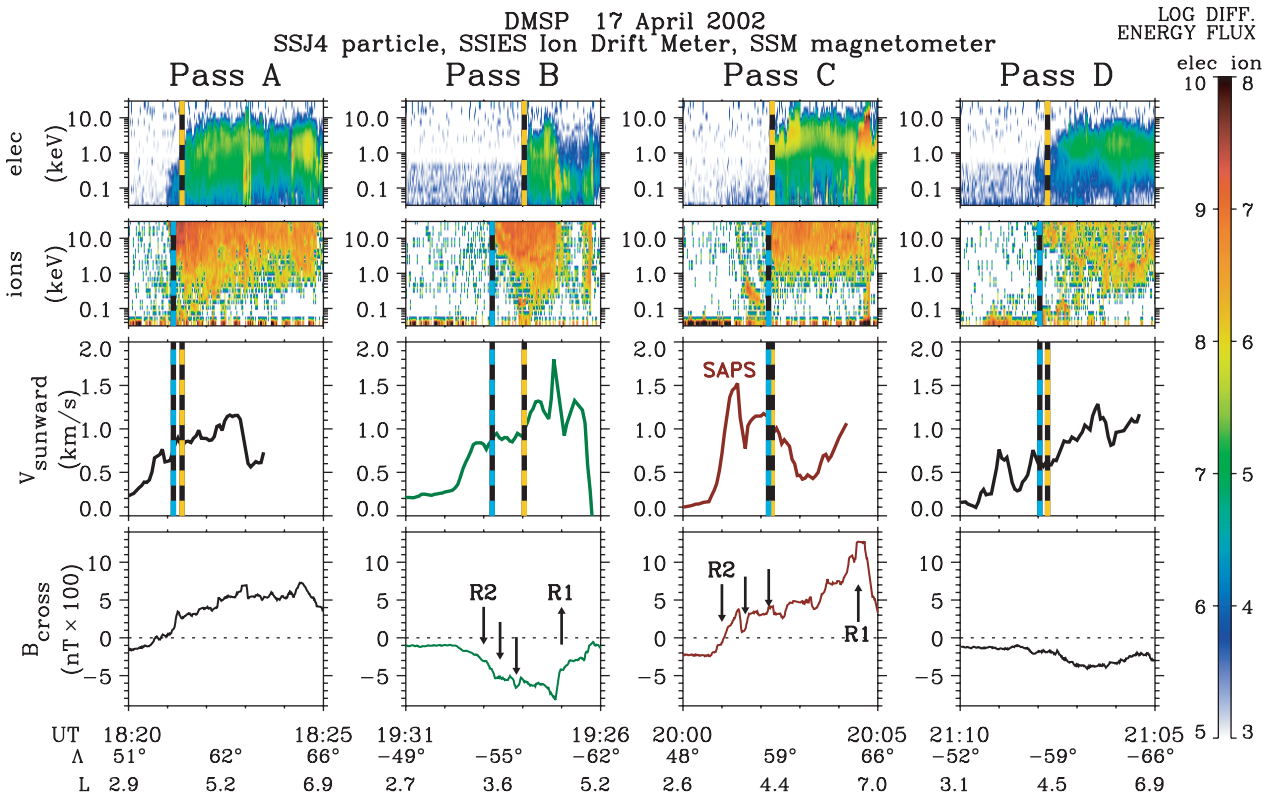

Figure 9. Data from four consecutive passes (labeled 'A' through 'D') of DMSP F13 satellite through duskside subauroral ionosphere between 1800 UT and 2100 UT. Passes A and C (B and D) were in the northern (southern) hemisphere. TOP TWO ROWS: electron and ion fluxes. The low-latitude edge of the electron (ion) precipitation is indicated in each plot by the thick yellow/black (blue/black) dashed line. The subauroral region is to the left of the yellow/black line. THIRD ROW: $V_{\rm sunward}$, the roughly sunward component of inertial-frame flow. BOTTOM ROW: $B_{\rm cross}$, the antisunward component of magnetic field. Region 2 ('R2') and region 1 ('R1') currents indicated, as described in the text.

particle detectors measure electron and ion fluxes in the energy range 0.1–30 keV. The DMSP SSIES ion drift meter measures the cross-track bulk plasma flow speed. Vector magnetic field data are obtained by the DMSP SSM fluxgate magnetometers. During 1800 UT to 2100 UT on 17 April the roughly dawn-dusk orbit of the DMSP Flight 13 (F13) satellite carried it through the duskside subauroral ionosphere four times. The SSJ4 particle, SSIES ion drift meter, and SSM magnetometer data from these four passes, labeled 'A' through 'D', are shown in Figure 9. Passes A and C were in the northern hemisphere, and passes B and D were in the southern hemisphere.

The top row shows electron fluxes; the middle row shows ion fluxes. After 1995, the SSJ4 instrument on the F13 satellite suffered degraded ability to detect low energy (below 1 keV) ions because of signal strength attenuation, causing an artificial roll-off in ion flux below 1 keV. The absence of signal at low energy does not mean there is no low-energy ion flux; however, the presence of low-energy ion fluxes does indicate (qualitatively) the presence of ions. The third row of Figure 9 plots $V_{\rm sunward}$, which is the component of flow perpendicular to the roughly dawn-dusk F13 trajectory. The eastward corotation speed has been subtracted from $V_{\rm sunward}$. The bottom row of Figure 9 shows $B_{\rm cross}$, the component of magnetic field perpendicular to the satellite trajectory in the antisunward direction; this component is useful for diagnosing the presence of field-aligned currents, which appear as gradients or excursions in $B_{\rm cross}$. The region 2 and region 1 current approximate locations are labeled (somewhat schematically, as discussed below) 'R2' and 'R1' in the bottom panels of Figure 9 for pass B and pass C. Text at the bottom of each column (i.e., each pass) indicates UT, magnetic latitude Λ and dipole L. In each plot, latitude increases to the right, so in pass B and pass D (during which F13 moved from high to low latitude) the UT ranges are reversed. In each plot the auroral precipitation zone contains high particle flux levels with a relatively well-defined low-latitude edge. The low-latitude edge of the electron precipitation is indicated in each plot by the thick yellow/black dashed line; similarly, a blue/black dashed line indicates the equatorward edge of the ion aurora. In each plot, the subauroral region is to the left of the yellow/black line.

Anderson et al. [2001] outlined the following mechanism for the formation of SAPS during substorms. About 10 minutes after substorm onset, the equatorward boundaries of the ion and electron precipitation separate, with the ion boundary moving equatorward of the electron boundary. The subsequent build-up of large pressure gradients in the substorm-injected ring current drives a current system consisting of downward region 2 field aligned current (FAC) in the ion precipitation region. The region 2 current is formed as the closure of the partial ring current (shown in Figure 8); the source population can have contributions from both precipitating ring current ions and upward-flowing thermal electrons from the ionosphere. The region 2 FACs flow poleward

as Pedersen currents through the subauroral ionosphere and emerge as upward region 1 FAC in the electron precipitation region. The poleward Pedersen current flowing through the low-conductivity subauroral ionosphere creates a strong poleward electric field. This poleward E-field drives westward flows (of order 1 km/s in the ionosphere) which make up the SAPS flow channel. The subauroral Pedersen conductivity is further reduced by the subauroral E-field and current via processes in the F layer (ion neutral collisions, fast chemistry and vertical transport) and the E layer (poleward transport of plasma resulting from collisions with the neutral atmosphere). Thus, an E-field/conductivity feedback process favors the growth of intense poleward E-fields and the reduction of conductivity in the subauroral ionosphere. As the substorm progresses, the ion and electron plasma sheet edges merge once again, and the region of subauroral current flow becomes latitudinally narrow, creating a spike signature at the inner edge of the SAPS flow channel (which should coincide with the inner edge of the ion plasma sheet). As the subauroral FACs diminish with the substorm recovery, the SAPS electric field is maintained by the depleted subauroral conductivity in the E and F layers of the ionosphere.

The DMSP plots in Figure 9 illustrate part of the SAPS formation scenario just described. During pass A (1820 UT to 1825 UT), the magnetic latitude (Λ) separation of the equatorward edges of the electron precipitation (top panel) and ion precipitation (middle panel) was minimal (about 0.8 degrees). At this time the subauroral flow speeds (bottom panel) were between 700 m/s and 900 m/s. About 30 minutes after the 1900 UT substorm onset, pass B (1926 UT to 1931 UT) shows a 2-degree Λ separation between the electron and ion precipitation regions, and the subauroral flow speeds below 55 degrees began increasing by a modest 100–200 m/s. The SSM magnetometer plot (bottom panel) of pass B shows the presence of the region 2 ('R2') downward field-aligned current after about 1928 UT, in the vicinity of the equatorward edge of the ion auroral precipitation; i.e., the SAPS current system began to form at this time. We identify pass B as the beginning of the formation of the SAPS flow channel in the zone between the inner edge of the region 2 FAC and the equatorward edge of the electron precipitation. By pass C (2000 UT to 2005 UT) a fully-developed SAPS flow channel was evident as sunward flow speeds of about 1 km/s or more, confined between 54°Λ–59°Λ, and possessing a narrow spike of high-speed (1.5 km/s) flow at the inner edge. The latitudinal extent of this SAPS channel spanned the subauroral ionosphere between the locations of the inner edge of the region 2 current ('R2' in the bottom panel of pass C in Figure 9) and of the equatorward edge of the aurora where the conductivity rose due to electron precipitation. In pass D (2105 UT to 2110 UT) this SAPS flow channel was gone.

Although DMSP data do support the SAPS interpretation, it should be noted that the edges of the precipitation regions in SSJ4 particle data are not an entirely robust indicator of the presence of field-aligned currents [*Heinemann et al.*, 1989]. This shortcoming is illustrated by pass C. In pass C, the equatorward edge of the ion precipitation (blue/black dashed line) coincided with the edge of the electron precipitation (yellow/black dashed line), and both edges were poleward of the main part of the SAPS flow channel. The presence of SAPS requires region 2 and region 1 FACs, connected through an ionospheric Pedersen current, so we expect to see evidence of the region 2 FAC near the inner edge of the SAPS flow channel. If we take the equatorward edge of the ion precipitation as the edge of the region 2 FAC, then there was no region 2 current to support the observed SAPS. However, the plot of $B_{\rm cross}$ shows a steep positive excursion (indicating strong region 2 current) at 2001 UT followed by a more gradual increase (indicating weaker region 2 current), and a negative excursion (indicating region 1 current) beginning at 2004:30 UT (at about 66 degrees latitude). The region 2 and region 1 current locations are schematically labeled 'R2' and 'R1' in Figure 9. The region 2 currents occupy much or all of the latitude range of the precipitating ions, as suggested by the multiple downward arrows. Thus, although the equatorward edge of the ion precipitation lies poleward of the equatorward edge of the SAPS region, the magnetic field data clearly indicate the presence of region 2 FAC at the SAPS equatorward edge. Note the isolated low-energy ion precipitation signature equatorward of the blue/black dashed line (see the orange blob before 2002 UT in the ion plot of pass C). This signature suggests that low-energy plasma, mostly invisible to the SSJ4 ion detector except for the 2002 UT blob, carried the region 2 FAC implied by the $B_{\rm cross}$ positive excursion at 2001 UT. It should be remembered that even very weak region 2 FAC, flowing into the extremely low conductivity of the nightside E and F layer subauroral ionosphere, can support the SAPS E-field. It is also worth noting that the poleward edge of the SAPS region coincides not with the region 1 FAC but rather with the location of the sharp change in conductivity at the equatorward auroral boundary. The poleward Pedersen current connecting region 2 (low latitude) and region 1 (high latitude) FAC flows beyond the high-latitude boundary of the SAPS region.

The DMSP observations can be related to the global observations we have already shown in previous sections. The interval of SAPS activity (within 1930–2100 UT) coincided with the second phase of the undulation, during which the indentation propagated westward and removed the outer 1 $R_{\rm E}$ of the duskside plasmasphere. The mean SAPS flow speed observed by DMSP during pass C between 54°Λ and 59°Λ was 1.2 km/s, consistent with the EUV-derived SAPS flow speed at that MLT and UT (Section 3.2.3). The SAPS activity happened subsequent to the build-up of ring current pressure that resulted from the substorm injection. It is likely that the ring current enhancement provided pressure gradients where region 2 FAC could close the circuit with the region 1 auroral FAC that had formed with the substorm (after 1900 UT). The main purpose of this DMSP/IMAGE comparison is that both sets of observations show the presence of SAPS; the motions of the equatorial plasmasphere and sub-auroral ionosphere were coupled together, and the formation of the SAPS was in turn due to coupling between the ring current and ionosphere. The good agreement between the EUV-inferred and DMSP-observed SAPS flow speeds lends confidence to this interpretation.

5.3. Synoptic View of SAPS

Figure 10 shows a schematic diagram of the SAPS effect, using a cartoon (on the left) and some plotted data (on the right). In the cartoon, the Earth is in the center, viewed from a dayside vantage point along the Earth-Sun line. Dawn is to the left; dusk is to the right. Dipole magnetic field lines are plotted at even (solid lines) and odd

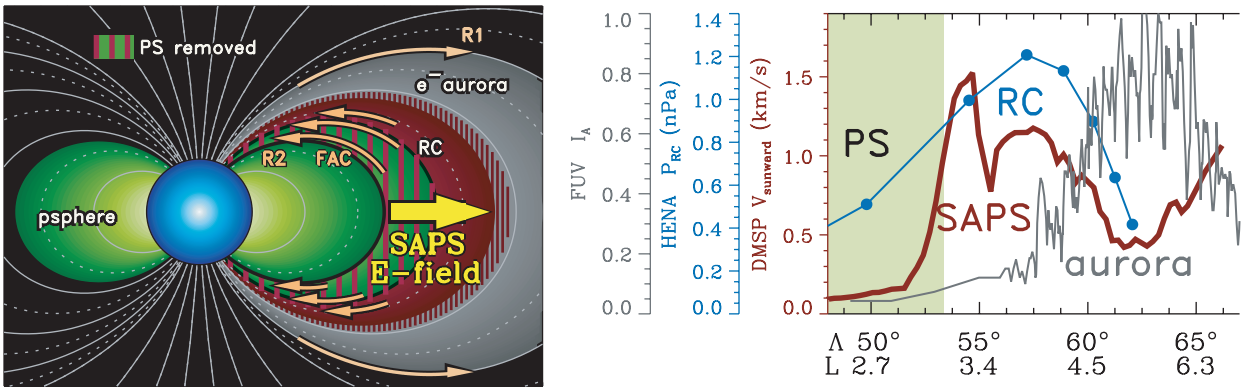

Figure 10. Schematic diagram of the SAPS effect. LEFT PANEL: Cartoon depicting plasmasphere ('psphere'), auroral electron plasmasheet ('e$^-$aurora'), partial ring current ('RC'), region 1 and 2 FAC, and SAPS electric field. Dawn (dusk) is to the left (right). RIGHT PANEL: Schematic plots of SAPS-related data. Radial cuts through images from IMAGE EUV (plasmasphere, 'PS') and IMAGE HENA (ring current, 'RC'), taken at 2024 MLT, mapped to the ionosphere. Latitudinal cut through IMAGE FUV image ('aurora') at 2024 MLT, and latitudinal cut through DMSP F13 drift meter data at 1827 MLT ('SAPS'). To the left of the plot are scales color-coded to each of the profiles.

(dotted lines) integer L values. The plasmasphere is depicted by the two green lobes near dawn and dusk. (The dawnside lobe is labeled 'psphere'.) The auroral electron plasma sheet ('e$^-$aurora') is the grey field-aligned region at the right of the plot. The partial ring current ('RC') is the maroon region between the electron plasma sheet and the plasmasphere. The SAPS electric field points radially outward and occupies the space between the inner edge of the region 2 currents (depicted as light orange arrows), and the electron plasma sheet inner edge (the maroon/gray cross-hatched area) where the ionospheric conductivity changes from low (in the subauroral zone) to high (in the auroral precipitation zone). Field lines in the SAPS region map to the subauroral ionosphere, where the conductivity is much lower than in the auroral zone. The SAPS E-field causes a strong westward flow (out of the plane of the diagram) that strips away the portion of the duskside plasmasphere that overlaps the SAPS region. The removal of plasmaspheric plasma by SAPS is schematically indicated by the green/maroon cross-hatched outer plasmaspheric (or inner ring current) zone. Given a few hours' time and a steady SAPS strength, the duskside plasmapause would roughly coincide with the inner edge of the SAPS flow channel, which also should approximately coincide with the inner edge of the RC. In an event like 17 April 2002, the SAPS strength is far from constant in time, explaining the overlap between the ring current and plasmapause in Figure 8.

The right side of Figure 10 schematically shows latitudinal/radial cuts through the plasmasphere ('PS'), ring current ('RC'), electron auroral plasma sheet ('aurora'), and SAPS flow channel ('SAPS'). The PS, RC, and aurora profiles are radial cuts through the equatorial IMAGE data at 2024 MLT and about 2007 UT. (This MLT was chosen somewhat arbitrarily to represent the post-dusk sector.) The plasmasphere is the filled green rectangle whose right edge is at $L = 3.3$ (obtained from the 2024 MLT plasmapause in Figure 2e). The ring current profile (blue curve) is a radial slice at 2024 MLT through the 2005 UT HENA proton pressure (Figure 8d), plotted versus Λ values that were computed using the Tsyganenko magnetic field model [*Tsyganenko*, 2002a, b]. The auroral profile (grey spiky curve) is a latitudinal slice through the polar-projected FUV image (Figure 6c), with L values computed using the Tsyganenko model. The SAPS profile (thick red curve) shows the DMSP sunward flow speed from pass C of Figure 9, obtained at about 1827 MLT. Note that the SAPS profile was taken from dusk rather than the pre-midnight 2024 MLT of the other profiles because DMSP observations of SAPS were not available at 2024 MLT. To the left of the plot are scales that are color-coded to each of the profiles; the FUV auroral intensity scale is in arbitrary (normalized) units.

The data on the right side of Figure 10 show how the IMAGE and DMSP data are consistent with the SAPS effect depicted in the left panel. The SAPS flow channel occupies the region between the auroral zone and the plasmasphere (PS). The outer edge of the plasmasphere coincides with the inner edge of the SAPS. The picture implies the presence of region 2 field aligned currents (FAC) in the L range of the ring current (RC), and region 1 FAC at the poleward edge of the auroral electron plasma sheet. Note that the location of the equatorward edge of the FUV-observed electron aurora (about 59 to 60 degrees latitude) agrees with the location observed by the DMSP SSJ4 electron detector in pass C of Figure 9. Also note that the location of the poleward edge of the FUV aurora (about 66 degrees latitude) agrees with the location of the region 1 FAC observed by the DMSP SSM magnetometer in pass C (Figure 9).

6. The Role of Reconnection

In the previous sections we showed a connection between the motion of the nightside plasmapause on 17 April 2002 and an auroral substorm that occurred after 1900 UT and led to the formation of a SAPS flow channel. Since decades of observations show that dayside magnetopause reconnection (DMR) generally plays a strong role in plasmaspheric dynamics, it is natural to examine the role of DMR-driven convection in the 17 April event.

Figure 11a plots $B_{z,IMF}$, the Z-component (in GSM coordinates) of the IMF, taken from the grey-shaded portion of Figure 1e. Negative $B_{z,IMF}$ in Figure 11a indicates the presence of dayside magnetopause reconnection. To relate the dayside reconnection to its effect on the inner magnetosphere, we calculated $E_{SW} \equiv V_{SW} B_{z,IMF}$, the dusk-to-dawn

solar wind electric field. Figure 11b shows $E_{\rm SW}$, delayed with respect to the magnetopause $B_{\rm z,IMF}$ by an additional 30 minutes to account for the time delay $\Delta\tau$ mentioned in Section 1. Negative $E_{\rm SW}$ corresponds to southward IMF and dayside reconnection; when $E_{\rm SW} < 0$, sunward convection is imposed the inner magnetosphere.

Figure 11c contains the azimuthal electric field E_φ obtained from IMAGE EUV plasmapause observations, averaged over the pre-midnight 2100–2400 MLT sector. Unlike the E_φ shown in Figure 4c, which was deduced by estimating $\dot{\varphi}$ from the ripple motion, E_φ from Figure 11c was calculated from Equation (1) with the assumption that the plasmapause radius was circular (approximately true in the pre-midnight sector), so that $E_\pi \approx E_\varphi$. Negative E_φ indicates inward plasmapause motion. The vertical dotted lines in Figures 11b and 11c mark where E_φ crossed zero.

The two intervals of negative E_φ, 1850–1922 UT and 1937–1959 UT, match up quite well with the intervals of negative $E_{\rm SW}$ in Figure 11b. Taken by itself, this correlation would imply that dayside reconnection was the dominant cause of the inward plasmapause motion. However, two things should be considered. First, before 1800 UT on 17 April, the IMF had been strongly southward for large portions of the day. After prolonged periods of southward IMF, the effectiveness of further southward IMF is reduced, because once depleted by erosion, the outer plasmasphere takes a long time (between several hours and a few days) to refill from the ionosphere. Second, we have already presented convincing evidence that the 1900 UT auroral substorm and the duskside SAPS played a crucial role in the plasmaspheric dynamics on 17 April. This is further demonstrated by examination of Figure 11d, containing FUV auroral intensity at midnight MLT (in arbitrary units), and Figure 11e, containing the peak duskside SAPS flow speed $V_{\rm sunward}$ recorded by the DMSP F13 satellite during the four successive passes (A, B, C, and D from Figure 9) through the subauroral 850-km ionosphere. The first interval of inward plasmapause motion can be correlated with the auroral intensity peak in Figure 5d, and the second interval can be correlated with the peak in the SAPS flow speed in Figure 5e. Note however that the shape of the second negative E_φ excursion (1937–1959 UT in Figure 11c) is closer to the shape of $E_{\rm SW}$ than that of $-V_{\rm sunward}$ during the same time period, and on average we expect SAPS to be stronger near dusk than midnight. So perhaps DMR-driven convection played a significant role close to midnight and after 1937 UT.

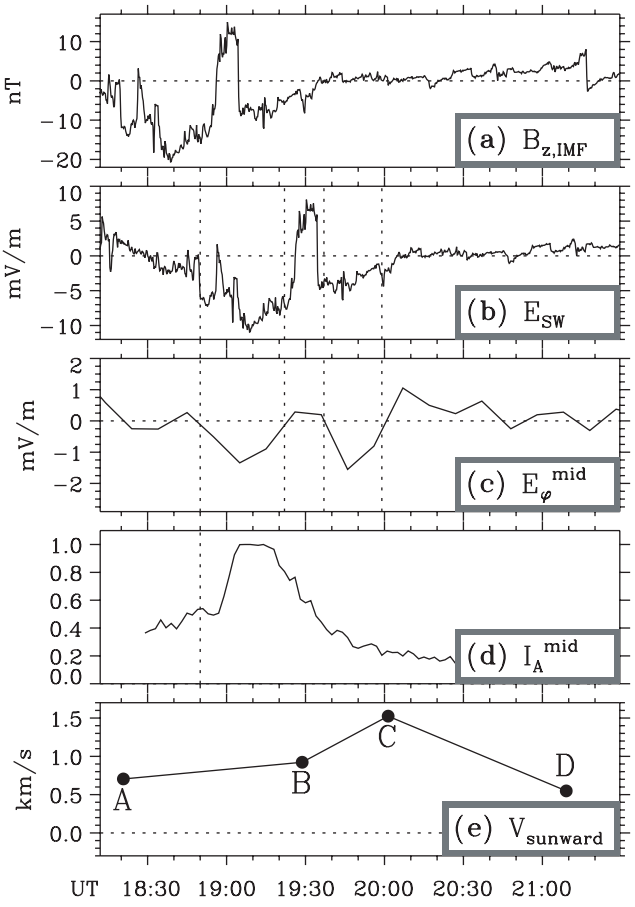

Figure 11. Assessment of the role of dayside magnetopause reconnection on 17 April 2002. Panel 11a: ACE $B_{\rm z,IMF}$. Panel 11b: $E_{\rm SW} \equiv V_{\rm SW} B_{\rm z,IMF}$, dusk-to-dawn solar wind electric field, delayed by 30 minutes (see text). Panel 11c: IMAGE EUV E_φ averaged over 2100–2400 MLT sector. Panel 11d: FUV auroral intensity at midnight MLT (arbitrary units). Panel 11e: Peak duskside SAPS flow speed $V_{\rm sunward}$ recorded by the DMSP F13 during four successive passes (A, B, C, and D from Figure 9).

The interval of positive $E_{\rm SW}$ between 1922 UT and 1937 UT overlaps the period of time during which the pre-SAPS mild bulge formed (i.e., 1915 UT to 1936 UT), so it is possible that antisunward convection due to overshielding [*Jaggi and Wolf*, 1973; *Kelley et al.*, 1979] contributed to the bulge formation. However, we do not believe overshielding played a significant role in the bulge formation, for the following reasons. First, the earliest outward plasmapause motion preceded the positive $E_{\rm SW}$ interval, precluding the influence of overshielding at the start of the bulge formation. Second, overshielding is believed to be a stronger effect on the dawnside, but no dawnside antisunward motion was observed during the mild bulge formation. On the other hand, overshielding may have been involved with the 2007–2017 UT plasmapause 'rebound' (Sections 3.1 and 3.2.2). Figure 11c shows that positive E_φ (outward plasmapause motion) occurred after 2007 UT, coincident with a gentle transition from negative to zero $E_{\rm SW}$, a transition that suggests reduction in the DMR-driven convection that might lead to overshielding.

In the following section, we offer an interpretation of all the observations we have presented in this paper.

7. Interpretation

In this paper we have presented both global images and in situ observations from 1800 UT to 2100 UT on 17 April 2002. Each section focused on a particular sub-region of the magnetosphere-ionosphere system. In this section, we attempt to synthesize the coupled responses of all the sub-regions.

We suggest the following sequence of events to explain the 17 April 2002 observations.

1. The substorm onset occurred at 1900 UT (Figure 7), perhaps triggered by the 1856 UT northward IMF turning at the magnetopause (Figure 11a). Subsequently, the dipolarization associated with the substorm onset induced sunward convection in the inner magnetosphere.

2. At the same time as the dipolarization, the time-delayed effects of the 1820 UT IMF southward turning (Figure 11a) and its initiation of dayside reconnection were felt as enhanced sunward convection at the nightside plasmapause between 1855 UT and 1905 UT (Figure 11b).

3. Together, the dipolarization and dayside reconnection contributed to create a sharp sunward convective impulse to the inner magnetosphere. We believe the substorm dipolarization dominated, for two reasons.

(i) The initial plasmapause indentation occurred in pre-midnight (Figure 4b), consistent with the onset location (Figure 6a). In other EUV observations of nightside plasmapause motion driven by dayside reconnection, initial sunward motion is usually found not at pre-midnight, but post-midnight (e.g., *Goldstein et al.* [2003a, 2004c]; *Goldstein and Sandel* [2004]). The different MLT location of the initial indentation for this event suggests a different origin of the convection, namely, the substorm.

(ii) The close [MLT, UT] correlation between the auroral and plasmapause ripple signatures (Figure 7) suggests very strongly that the auroral substorm, and not dayside reconnection, dominated the early plasmapause evolution.

4. The sunward convective impulse caused a ring current injection in the pre-midnight MLT sector (Figure 8a).

5. The impulse also distorted the shape of the plasmapause (Figures 2, 4, and 5). The pre-midnight plasmapause was indented by the first approach of the impulse. As the impulse traveled sunward, the initial plasmapause indentation widened, leaving reduced plasmapause radius in its wake. The eastern and western edges of the widening indentation were marked by ripples; i.e., azimuthal gradients in the plasmapause radius.

6. The build-up of ring current pressure associated with the injection produced at least one, and possibly two, effects.

(i) The enhanced ring current pressure may have caused a reduction in the strength of the pre-midnight geomagnetic field, causing the cold plasmaspheric plasma to flow antisunward there. This antisunward motion could account for the formation of the pre-SAPS mild bulge during the interval from 1915 UT to 1936 UT (Figures 2b, 4e, and 4f). The formation of this mild bulge was the first phase of the duskside plasmapause undulation.

(ii) At 1930 UT, enhanced ring current pressure provided a source for region 2 field aligned currents to flow into the ionosphere at the inner edge of the ring current. From there, the current flowed poleward through the subauroral ionosphere, to join with region 1 FAC flowing out of the ionosphere in the auroral zone. The creation of this current system (depicted in Figure 9, pass B) produced the subauroral polarization stream, or SAPS (Figures 9 and 10).

7. On the duskside, the sunward motion was further enhanced by westward SAPS flows. After about 1930 UT the duskside dynamics were apparently dominated by the SAPS electric field, which carved away the outer 1 R_E of the duskside plasmasphere in the second phase of the large duskside plasmapause undulation effect (Figures 2 and 4).

8. On the duskside the plasmapause ripple, the peak in the ring current pressure, and the substorm auroral signature all moved westward at roughly the same rate (Figures 6, 7, and 8).

(i) The auroral motion may indicate that auroral precipitation is intensified at the sunward-moving location of the dipolarization front.

(ii) The ring current and plasmaspheric plasma moved in response to the impulse provided by the dipolarization front.

This scenario, consistent with all the observations we have presented, involves multiple contributions and coupling among various components of the magnetosphere-plasmasphere-ionosphere system. The chain of events involves some element of coincidence. The 1856 UT northward IMF turning triggered the substorm at almost the same time as the 30-minute-delayed effect of the 1820 UT southward IMF turning reached the nightside plasmapause. This coincidence may simply arise from the fact that the southward IMF interval lasted about 30 minutes.

Previously reported EUV observations of the active-time plasmasphere have shown the effects of enhanced sunward convection that is directly driven by dayside magnetopause reconnection (DMR) during southward IMF [*Goldstein et al.*, 2003a; *Spasojević et al.*, 2003]. In typical DMR-driven events, substantial plasmasphere erosion occurs as a result of sustained, enhanced sunward convection. The 17 April 2002 event is the first case in which the EUV-observable effect of substorm dipolarization has been identified. In contrast to the erosion that typically results from sustained southward IMF, the dipolarization apparently caused a transient sunward convective impulse to sweep past the plasmasphere, temporarily distorting the plasmapause. Part of the transient effect was an initial partial plasmapause indentation that subsequently expanded to include an increasingly wider range of MLT. *Goldstein and Sandel* [2004] argued that this UT-MLT-dependent indentation effect is probably a normal component of erosion as well, although difficult to spot without E-field analysis such as performed in Section 3.2.2. This subtler partial indentation effect may be the only plasmaspheric signature of substorm dipolarization, which may explain why plasmaspheric effects of substorms have not previously been identified in EUV images despite the frequency of substorm occurrence.

The most dramatic effect of the 17 April event was the duskside undulation, and it was the identification of this undulatory plasmapause motion that spurred further investigation of the event. The circumstances leading to the undulation formation involved a closely-linked chain of events: ring current pressure buildup led to magnetic inflation which created a mild plasmaspheric bulge that was subsequently stripped away by SAPS (which in turn formed due to the same ring current pressure enhancement). The 17 April 2002 undulation is the only observation of its type that has been identified to date, and it may prove a unique occurrence. However, because the chain of events involved such strong internal magnetospheric-ionospheric coupling, it may be an intrinsic inner magnetospheric behavior pattern. We suspect that other similar events will indeed be found in EUV images now that this phenomenon has been discovered.

8. Summary and Conclusions

The IMAGE mission was conceived with the idea that multiple instruments could obtain a global, comprehensive picture of the entire magnetosphere-ionosphere system. Aided by the availability of in situ measurements, the IMAGE observations of the 17 April 2002 event suggest strong coupling between the plasmasphere and the other plasma populations of the inner magnetosphere during a substorm that occurred in the recovery phase of the 17 April storm. This coupling allows the plasmasphere to serve as a diagnostic of the plasma sheet-ring current-ionosphere interplay.

IMAGE FUV images show a substorm onset at 1900 UT in the pre-midnight MLT sector. Both the ring current and the plasmasphere responded to this 1900 UT onset, which presumably involved a global dipolarization of the nightside magnetotail. After 1900 UT, IMAGE HENA observed a ring current injection between 2100 MLT and 2400 MLT; this injection doubled the pre-substorm proton pressure in the 10–60 keV energy range. Between 1855 UT and 1905 UT, IMAGE EUV observed a 0.2–0.3 R_E indentation of the plasmapause in the 2100–2400 MLT range; this indentation subsequently widened to other MLTs. The substorm onset occurred in the same MLT range, and at the same time (taking into account the different image cadences of FUV, HENA, and EUV) as the ring current injection and plasmapause indentation.

The EUV plasmasphere observations suggest that the substorm dipolarization produced a global convective impulse that propagated sunward at about 3.6 km/s, consistent with prior measurements of substorm injection front speeds [*Reeves et al.*, 1996]. The sunward impulse of the dipolarization effect distorted the plasmapause shape. Behind the leading edge ('front') of the impulse, the plasmapause radius was reduced, producing partial indentation of the nightside plasmapause. As the front traveled sunward, the plasmapause indentation widened, expanding both eastward and westward. At the MLT edges of this widening indentation, the plasmapause bulged outward, forming ripples that we assume coincided with the time-dependent location of the impulse front. There is some evidence that the plasmapause radius bulged outward ahead of the moving front, which we suggested might be due to a 'snowplow' effect in which plasma removed from the nightside by the sunward convection was diverted around and outside the pre-existing plasmapause, causing a local increase in the plasmapause radius there. The MLT-UT rate of progress of the ripples was the same as that of the substorm-associated auroral signatures on both dawnside and duskside. The westward progress of the duskside ripple was the same as that of the ring current pressure peak. The close correspondence between the ripples (i.e., the front location) and the aurora might mean that auroral precipitation is intensified at the location of a sunward-moving impulse front. The agreement between the plasmapause ripples and the ring current distribution probably means that both ring current plasma and plasmaspheric plasma were being driven in unison by the convection E-field. It may be true that the SAPS effect did not occur simultaneously at all MLTs in the dusk-to-midnight MLT sector, but rather propagated westward with both ring current and aurora. The presence of SAPS requires both region 2 and region 1 FAC, so if either or both of the aurora and ring current are moving, the SAPS effect might occupy only the time-varying location where both FAC systems are in place.

The combination of two effects, the plasmapause indentation and the motion of the ripples along the plasmapause, allowed us to extend the technique of *Goldstein et al.* [2004c] and estimate the total vector electric field at the moving plasmapause. The inferred vector E-fields demonstrate that there can be a significant difference between the motion of the plasmapause boundary and the motion of the plasma that lies inside or along that boundary. The EUV-deduced E-fields can be used to analyze boundary motion that arises from either compressional (radial) or erosional (azimuthal) plasma motions.

In the dusk-to-midnight MLT sector, the westward propagating ripple created a dramatic plasmapause undulation effect, as first reported by *Goldstein et al.* [2004a]. The undulation consisted of two phases. In the first phase (1915 UT to 1936 UT) of the undulation, the pre-midnight plasmapause moved outward to form a mild 0.4–0.5 R_E bulge centered at 2000 MLT. The origin of this bulge is uncertain. We speculated that the post-injection, pre-midnight ring current pressure increase caused a local reduction in the geomagnetic field strength, inducing an electric field which pulled the plasmapause in the antisunward direction, creating the bulge. A crude calculation of the electric field that might arise from such a magnetic reduction was consistent with the 1-to-2 mV/m EUV-inferred tangential electric field (E_π) strength associated with the bulge formation. The EUV E_π signature suggests eastward (antisunward) plasma motion during the bulge formation, which is weakly supported by quantitatively comparable eastward motion of an auroral signature in FUV data.

In the second phase of the undulation, the mild pre-midnight bulge that formed in the first phase was removed by a sharp indentation/ripple that propagated westward along the midnight-to-dusk plasmapause, stripping away the outer 1 R_E edge of the plasmasphere. All evidence supports the interpretation that this second phase of the undulation was caused by the subauroral polarization stream (SAPS), a radially-confined westward/outward flow channel typically found in the dusk-to-midnight MLT sector. The ring current, subauroral ionosphere, and aurora were together involved in the creation of the SAPS electric field. We believe that after 1930 UT, the enhanced ring current pressure (due to the injection) provided plasma pressure gradients that drove region 2 field aligned currents (FAC). The region 2 FAC linked to the region 1 auroral FAC via poleward Pedersen currents in the low-conductivity subauroral ionosphere, creating the intense poleward SAPS E-field. The birth and death of the SAPS flow channel, with its accompanying ionospheric current system, was observed in the 850-km-altitude topside ionosphere by the DMSP F13 satellite. The DMSP-observed UT interval of SAPS activity coincided with the EUV observations of the second undulation phase. At about 1930 UT the DMSP data show that the the ion precipitation region and region 2 FAC both moved equatorward of the electron precipitation region, creating the SAPS effect, in accord with the known SAPS formation scenario [*Anderson et al.*, 2001]. According to DMSP ion drift meter data, during 2000 UT to 2005 UT the fully-developed SAPS flow channel was characterized by westward flows with an average speed of 1.2 km/s and a peak speed of 1.5 km/s. Equatorial electric fields inferred from EUV images suggest the presence of a SAPS flow channel in the interval 1936 UT to 2037 UT. In this EUV-inferred SAPS channel, flows were directed westward and outward in the dusk-to-midnight MLT sector (in agreement with average SAPS properties) and flow speeds were about 5 R_E/hour, which when mapped to the ionosphere corresponds to about 1.2 km/s. This 5 R_E/hour SAPS speed is somewhat larger than the < 1 R_E/hour speeds observed during plasmasphere erosion that is driven by dayside magnetopause reconnection [*Goldstein et al.*, 2003a].

Combining IMAGE and DMSP data, the global picture of the SAPS effect on 17 April 2002 is as follows. The SAPS flow channel occupied the region between the inner edge of

the auroral zone and the inner edge of the partial ring current. The SAPS flows carved away the outer 1 R_E layer of the plasmasphere, so that over time the plasmapause moved inward toward the SAPS inner edge. DMSP magnetometer data showed the presence of region 2 FAC at the inner gradient of the HENA ring current pressure distribution, and region 1 FAC at the poleward edge of the auroral electron plasma sheet.

To explain the traveling ripple effect on the plasmapause, including the very dramatic duskside plasmapause undulation between 1936 UT and 2037 UT, it is necessary to consider the influences of the auroral plasma sheet, ring current, and ionosphere. The substorm dipolarization initiated the event, causing sunward convection which affected both plasmasphere and ring current. The ring current apparently distorted the geomagnetic field, producing a mild pre-midnight plasmapause bulge. The ring current then coupled to the ionosphere to produce SAPS, which enhanced the duskside sunward convection and removed the mild bulge. It was the formation and removal of this mild bulge that produced the plasmapause undulation on the duskside. This event represents the first identification of the directly-observed effects on the plasmasphere of both (A) a finite-speed propagating convective impulse (which we assume is due to substorm dipolarization) and (B) the SAPS flow channel. It is possible that the plasmaspheric effect of induction electric field, due to magnetic field reduction by the ring current, was also first identified in this event.

The benefit of multi-instrument, multi-satellite study of the inner magnetosphere has been demonstrated, and this type of study should be pursued for other events in the future. The Earth's magnetosphere is a complex, coupled system in which there are dynamic linkages between different plasma regions. The strength of magnetospheric imaging is its ability to provide global information that is required to unambiguously determine causal relationships that interconnect the plasmasphere, ionosphere, aurora, and ring current. When combined with available in situ data for "ground truth" information, the strength of imaging is increased. Our analysis allowed us to examine a particular chain of coupled interactions of selected plasma populations, but much more work needs to be done toward a complete picture of the inner magnetosphere during substorms.

Acknowledgments.
The Dst, Sym-H, and Kp indices were provided by the World Data Center for Geomagnetism (WDC-C2) website, maintained by Kyoto University, Japan. Browse AE and AU indices were also examined on the Kyoto WDC-C2 site. The DMSP SSJ4 particle detectors were designed by D. Hardy of Air Force Research Laboratory, and data were obtained from Johns Hopkins University Applied Physics Laboratory. We thank D. Hardy, F. Rich, and P. Newell for the use of SSJ4 data. We are grateful to F. Rich for providing DMSP SSM magnetometer data, and discussing its interpretation. A discussion with P. Anderson about SAPS and field-aligned currents was also particularly useful. S. Fuselier provided equatorial maps of IMAGE FUV images that were useful in the preliminary analysis of the aurora for this event. We thank N. Ness, C. Smith, D. McComas, and the ACE science center for the easy availability of the ACE data set. We are indebted to R. Spiro for his suggestion of the pre-SAPS bulge formation method, and for his help interpreting DMSP data. Financial support was provided by the following grants: NASA SEC-GI NAG5-12787 (JG); NASA NAS5-96020 (JLB, JG, BRS, SBM); NASA NAG5-12772 (PCB); NAG5-9297 (MRH).

References

Aggson, T. L., J. P. Heppner, and N. C. Maynard (1983), Observations of large magnetospheric electric fields during the onset phase of a substorm, *J. Geophys. Res.*, *88*, 3981.

Akasofu, S.-I. (1964), The development of the auroral substorm, *Planet. Space Sci.*, *12*, 273.

Anderson, P. C., D. L. Carpenter, K. Tsuruda, T. Mukai, and F. J. Rich (2001), Multisatellite observations of rapid subauroral ion drifts (SAID), *J. Geophys. Res.*, *106*, 29585.

Arnoldy, R. L., and K. W. Chan (1969), Particle substorms observed at the geostationary orbit, *J. Geophys. Res.*, *74*, 5019.

Baker, D. N., T. I. Pulkkinen, V. Angelopoulos, W. Baumjohann, and R. L. McPherron (1996), Neutral line model of substorms: Past results and present view, *J. Geophys. Res.*, *101*, 12975.

Baker, D. N., et al. (1982), Observations and modelling of energetic particles at synchronous orbit on July 29,1977, *J. Geophys. Res.*, *87*, 5917.

Burch, J. L. (2000), IMAGE mission overview, *Space Sci. Rev.*, *91*, 1.

Burke, W. J., A. G. Rubin, N. C. Maynard, L. C. Gentile, P. J. Sultan, F. J. Rich, O. de La Beujardière, C. Y. Huang, and G. R. Wilson (2000), Ionospheric disturbances observed by DMSP at middle to low latitudes during the magnetic storm of June 4–6, 1991, *J. Geophys. Res.*, *105*, 18391.

Burke, W. J., et al. (1998), Electrodynamics of the inner magnetosphere observed in the dusk sector by CRRES and DMSP during the magnetic storm of June 4–6, 1991, *J. Geophys. Res.*, *103*, 29399.

Carpenter, D. L., and A. J. Smith (2001), The study of bulk plasma motions and associated electric fields in the plasmasphere by means of whistler-mode signals, *J. Atmos. Solar-Terr. Phys.*, *63*, 1117.

Carpenter, D. L., K. Stone, J. C. Siren, and T. L. Crystal (1972), Magnetospheric electric fields deduced from drifting whistler paths, *J. Geophys. Res.*, *77*, 2819.

Coroniti, F. V., and C. F. Kennel (1973), Can the ionosphere regulate magnetospheric convection?, *J. Geophys. Res.*, *78*, 2837.

C:son Brandt, P., R. DeMajistre, E. C. Roelof, S. Ohtani, D. G. Mitchell, and S. B. Mende (2002), Global ENA imaging of the plasmasheet and ring current during substorms, *J. Geophys. Res.*, *107*(A12), 1454, doi:10.1029/2002JA009307.

Demajistre, R., E. C. Roelof, P. C:son Brandt, and D. G. Mitchell (2004), Retrieval of global magnetospheric ion distributions from high energy neutral atom (ENA) measurements by the IMAGE/HENA instrument, *J. Geophys. Res.*, in press, doi:10.1029/2003JAo10322.

Dungey, J. W. (1961), Interplanetary magnetic field and the auroral zones, *Phys. Rev. Lett.*, *6*, 47.

Erickson, G. M., N. C. Maynard, W. J. Burke, G. R. Wilson, and M. A. Heinemann (2000), Electromagnetics of substorm onsets in the near-geosynchronous plasma sheet, *J. Geophys. Res.*, *105*(A11), 25265, doi:10.1029/1999JA000424.

Foster, J. C., and W. J. Burke (2002), SAPS: A new categorization for sub-auroral electric fields, *EOS Trans. AGU*, *83*, 393.

Foster, J. C., and H. B. Vo (2002), Average characteristics and activity dependence of the subauroral polarization stream, *J. Geophys. Res.*, *107*(A12), 1475, doi:10.1029/2002JA009409.

Foster, J. C., P. J. Erickson, A. J. Coster, and J. Goldstein (2002), Ionospheric signatures of plasmaspheric tails, *Geophys. Res. Lett.*, *29*(13), 1623, doi:10.1029/2002GL015067.

Friedel, R. H. W., A. Korth, and G. Kremser (1996), Substorm onset observed by CRRES: Determination of energetic particle source region, *J. Geophys. Res.*, *101*, 13137.

Goldstein, J., and B. R. Sandel (2004), The global pattern of evolution of plasmaspheric drainage plumes, in *Global Physics of the Coupled Inner Magnetosphere*, edited by M. Schulz, H. Spence, and J. L. Burch, American Geophysical Union, Washington, D. C., in press, PDF available at http://enarc.space.swri.edu/PAPERS/PUBs/pa_reprint_submitted.pdf.

Goldstein, J., B. R. Sandel, W. T. Forrester, and P. H. Reiff (2003a), IMF-driven plasmasphere erosion of 10 July 2000, *Geophys. Res. Lett.*, *30*(3), doi:10.1029/2002GL016478.

Goldstein, J., B. R. Sandel, P. H. Reiff, and M. R. Hairston (2003b), Control of plasmaspheric dynamics by both convection and sub-auroral polarization stream, *Geophys. Res. Lett.*, *30*(24), 2243, doi:10.1029/2003GL018390.

Goldstein, J., M. Spasojević, P. H. Reiff, B. R. Sandel, W. T. Forrester, D. L. Gallagher, and B. W. Reinisch (2003c), Identifying the plasmapause in IMAGE EUV data using IMAGE RPI in situ steep density gradients, *J. Geophys. Res.*, *108*(A4), 1147, doi:10.1029/2002JA009475.

Goldstein, J., B. R. Sandel, M. R. Hairston, and S. B. Mende (2004a), Plasmapause undulation of 17 April 2002, *Geophys. Res. Lett.*, *31*, L15801, doi:10.1029/2004GL019959.

Goldstein, J., B. R. Sandel, M. F. Thomsen, M. Spasojević, and P. H. Reiff (2004b), Simultaneous remote-sensing and in situ observations of plasmaspheric drainage plumes, *J. Geophys. Res.*, *109*, A03202, doi:10.1029/2003JA010281.

Goldstein, J., R. A. Wolf, B. R. Sandel, and P. H. Reiff (2004c), Electric fields deduced from plasmapause motion in IMAGE EUV images, *Geophys. Res. Lett.*, *31*(1), L01801, doi: 10.1029/2003GL018797.

Harang, L. (1951), *The Aurorae*, John Wiley & Sons, New York.

Heinemann, N. C., M. S. Gussenhoven, D. A. Hardy, F. Rich, and H.-C. Yeh (1989), Electron/ion precipitation differences in relation to region 2 field-aligned currents, *J. Geophys. Res.*, *94*, 13593.

Henderson, M. G., et al. (1997), First energetic neutral atom images from Polar, *Geophys. Res. Lett.*, *24*, 1167.

Jaggi, R. K., and R. A. Wolf (1973), Self-consistent calculation of the motion of a sheet of ions in the magnetosphere, *J. Geophys. Res.*, *78*, 2852.

Kan, J. R., and W. Sun (1996), Substorm expansion phase caused by an intense localized convection imposed on the ionosphere, *J. Geophys. Res.*, *101*, 21697.

Kelley, M. C., B. G. Fejer, and C. A. Gonzales (1979), An explanation for anomalous ionospheric electric fields associated with a northward turning of the interplanetary magnetic field, *Geophys. Res. Lett.*, *6*, 301.

Liemohn, M. W., A. J. Ridley, D. L. Gallagher, D. M. Ober, and J. U. Kozyra (2004), Dependence of plasmaspheric morphology on the electric field description during the recovery phase of the 17 April 2002 magnetic storm, *J. Geophys. Res.*, *109*, doi:10.1029/2003JA010304.

Lui, A. T. Y. (1996), Current disruption in the earth's magnetosphere: Observations and models, *J. Geophys. Res.*, *101*, 13067.

Lyons, L. R. (1995), A new theory for magnetospheric substorms, *J. Geophys. Res.*, *100*, 19065.

McIlwain, C. E. (1974), Substorm injectin boundaries, in *Magnetospheric physics: Proceedings of the Summer Advanced Study Institute,* Sheffield, England, 13–24 August 1973, p. 143, D. Reidel Publishing Co., Dordrecht.

Mende, S. B., et al. (2000), Far ultraviolet imaging from the IMAGE spacecraft. 3. Spectral imaging of Lyman-α and OI 135.6 nm, *Space Sci. Rev.*, *91*, 287.

Mitchell, D. G., et al. (2000), High energy neutral atom (HENA) imager for the IMAGE mission, *Space Sci. Rev.*, *91*, 67.

Moldwin, M. B., B. R. Sandel, M. Thomsen, and R. Elphic (2003), Quantifying global plasmaspheric images with in situ observations, *Space Sci. Rev.*, *109*, 47.

Ohtani, S., S. Kokubun, and C. T. Russell (1992), Radial expansion of the tail current disruption during substorms: A new approach to the substorm onset region, *J. Geophys. Res.*, *97*, 97.

Reeves, G. D., M. G. Henderson, P. S. McLachlan, R. D. Belian, R. H. W. Friedel, and A. Korth (1996), Radial propagation of substorm injections, in *Proceedings of the Third International Conference on Substorms* Versailles, France 12–17 May 1996, ESA SP-389, p. 579, European Space Agency.

Rich, F. J., and M. R. Hairston (1994), Large-scale convection patterns observed by DMSP, *J. Geophys. Res.*, *99*, 3827.

Roelof, E. C. (1987), Energetic neutral atom image of a storm-time ring current, *Geophys. Res. Lett.*, *14*, 652.

Roelof, E. C., and A. J. Skinner (2000), Extraction of ion distributions from magnetospheric ENA and EUV images, *Space Sci. Rev.*, *91*, 437.

Sandel, B. R., R. A. King, W. T. Forrester, D. L. Gallagher, A. L. Broadfoot, and C. C. Curtis (2001), Initial results from the IMAGE extreme ultraviolet imager, *Geophys. Res. Lett.*, *28*, 1439.

Sandel, B. R., J. Goldstein, D. L. Gallagher, and M. Spasojević (2003), Extreme ultraviolet imager observations of the structure and dynamics of the plasmasphere, *Space Sci. Rev.*, *109*, 25.

Sandel, B. R., et al. (2000), The extreme ultraviolet imager investigation for the IMAGE mission, *Space Sci. Rev.*, *91*, 197.

Singer, H. J., W. J. Hughes, C. Gelpi, and B. G. Ledley (1985), Magnetic disturbances in the vicinity of synchronous orbit and the substorm current wedge: A case study, *J. Geophys. Res.*, *90*, 9583.

Spasojević, M., J. Goldstein, D. L. Carpenter, U. S. Inan, B. R. Sandel, M. B. Moldwin, and B. W. Reinisch (2003), Global response of the plasmasphere to a geomagnetic disturbance, *J. Geophys. Res.*, *108*(A9), 1340, doi:10.1029/2003JA009987.

Stone, E. C., A. M. Frandsen, R. A. Mewaldt, E. R. Christian, D. Margolies, J. F. Ormes, and F. Snow (1998), The Advanced Composition Explorer, *Space Sci. Rev.*, *86*, 1.

Tsyganenko, N. A. (2002a), A model of the near magnetosphere with a dawn-dusk asymmetry: 1. Mathematical structure, *J. Geophys. Res.*, *107*(A8), 1179, doi: 10.1029/2001JA000219.

Tsyganenko, N. A. (2002b), A model of the near magnetosphere with a dawn-dusk asymmetry: 2. Parameterization and fitting to observations, *J. Geophys. Res.*, *107*(A8), 1176, doi: 10.1029/2001JA000220.

Vagina, L. I., V. A. Sergeev, D. N. Baker, and H. J. Singer (1996), Use of mid-latitude magnetic data for modeling and diagnostics of magnetospheric substorms, *Adv. Space Res.*, *18*(8), 229.

Vallat, C., I. Dandouras, P. C:son Brandt, and D. G. Mitchell (2004), First comparison between ring current measurements by cluster/CIS and IMAGE/HENA, *J. Geophys. Res.*, in press.

Walker, R. J., K. N. Erickson, R. L. Swanson, and J. R. Winckler (1976), Substorm-associated particle boundary motion at synchronous orbit, *J. Geophys. Res.*, *81*, 5541.

J. Goldstein, J. L. Burch, Southwest Research Institute, 6220 Culebra Road, San Antonio, TX 78228 USA (jgoldstein@swri.edu)

B. R. Sandel, Lunar and Planetary Lab, University of Arizona, Tucson, AZ 85721 USA

S. B. Mende, U. California Berkeley, Space Sciences Lab, 7 Gauss Way, Berkeley, CA 94720 USA

P. C:son Brandt, Johns Hopkins University Applied Physics Lab, 11100 Johns Hopkins Rd, Laurel, MD 20723 USA

M. R. Hairston, U.T. Dallas, P.O. Box 830688 FO22, Richardson, TX 75083 USA

(Received _____.)